Cell Biomaterials

Article

NIR-responsive hydrogenated TiO_2 nanoscale honeycomb surface pattern for rapid *S. aureus* biofilm elimination and enhanced osteogenesis

Graphical abstract

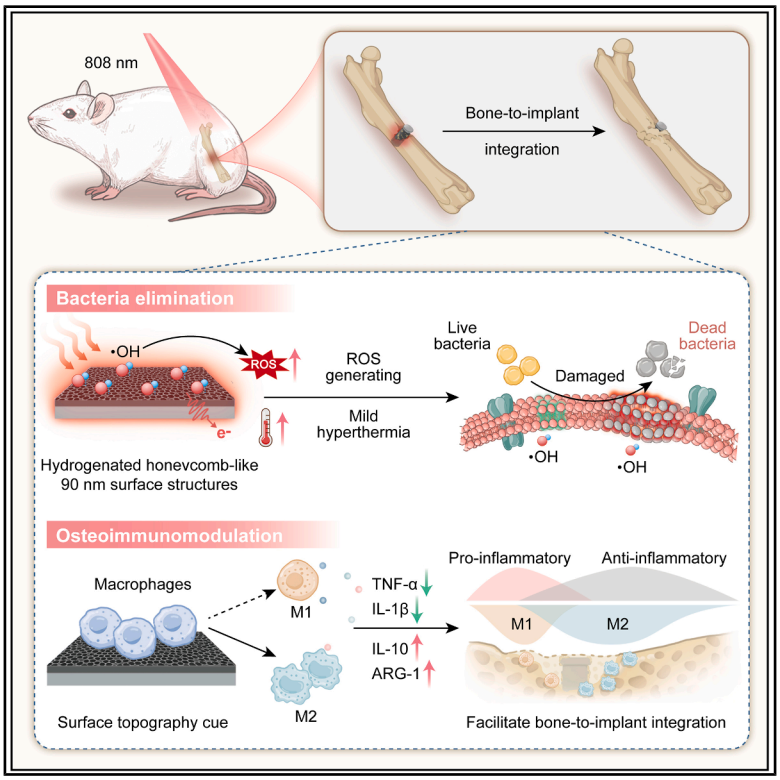

Highlights

- Engineered TiO_2 structure enables NIR-triggered rapid elimination of bacteria
- Nanoscale honeycomb topography guides osteoimmunomodulation
- Agent-free surface modification achieves both infection control and osseointegration

Authors

Yizhou Zhu, Jiajun Qiu, Can Ai, ..., Xin Zhao, Bin Li, Kelvin W.K. Yeung

Correspondence

liuxiangmei@hebut.edu.cn (X.L.), slwu@pku.edu.cn (S.W.), xyliu@mail.sic.ac.cn (X.L.), wkkyeung@hku.hk (K.W.K.Y.)

In brief

A hydrogenated TiO_2 nanoscale honeycomb surface pattern on titanium implants generates ROS and mild hyperthermia under NIR light, rapidly eradicating *S. aureus* biofilms. The 90-nm honeycomb topography directs macrophage polarization toward a pro-osteogenic phenotype, enhancing bone-to-implant integration. By integrating defect engineering and nanoscale honeycomb-like topography, this surface provides a clinically translatable solution for infection control and improved bone healing in implant-related applications.

Zhu et al., 2025, Cell Biomaterials *1*, 100213
December 23, 2025
https://doi.org/10.1016/j.celbio.2025.100213

CellPress

Please cite this article in press as: Zhu et al., NIR-responsive hydrogenated TiO_2 nanoscale honeycomb surface pattern for rapid *S. aureus* biofilm elimination and enhanced osteogenesis, Cell Biomaterials (2025), https://doi.org/10.1016/j.celbio.2025.100213

Cell Biomaterials

CellPress
OPEN ACCESS

Article

NIR-responsive hydrogenated TiO_2 nanoscale honeycomb surface pattern for rapid *S. aureus* biofilm elimination and enhanced osteogenesis

Yizhou Zhu,[1,2] Jiajun Qiu,[4] Can Ai,[1,2,5] Yiming Xiang,[1,2,3] Congyang Mao,[1,2,3] Jun Wu,[1,2] Wei Qiao,[1,2,6] Xiangmei Liu,[3,7,*] Shuilin Wu,[3,8,*] Xuanyong Liu,[4,9,*] Xin Zhao,[10] Bin Li,[11] and Kelvin W.K. Yeung[1,2,12,*]

[1]Department of Orthopaedics & Traumatology, Li Ka Shing Faculty of Medicine, The University of Hong Kong, Pokfulam, Hong Kong 999077, China
[2]Shenzhen Key Laboratory for Innovative Technology in Orthopaedic Trauma, Department of Orthopaedics and Traumatology, The University of Hong Kong, Shenzhen Hospital, Shenzhen 518053, China
[3]Biomedical Materials Engineering Research Center, Collaborative Innovation Center for Advanced Organic Chemical Materials Co-constructed by the Province and Ministry, Hubei University, Wuhan 430062, China
[4]State Key Laboratory of High Performance Ceramics and Superfine Microstructure, Shanghai Institute of Ceramics, Chinese Academy of Sciences, Shanghai 200050, China
[5]Department of Neonatology, Nanfang Hospital, Southern Medical University, Guangzhou 510515, China
[6]Dental Materials Science, Applied Oral Sciences, Faculty of Dentistry, The University of Hong Kong, Hong Kong 999077, China
[7]School of Health Science and Biomedical Engineering, Hebei University of Technology, Tianjin 300401, China
[8]School of Materials Science and Engineering, Peking University, Beijing 100871, China
[9]State Key Laboratory for Modification of Chemical Fibers and Polymer Materials, College of Biological Science and Medical Engineering, Donghua University, Shanghai 201620, China
[10]Department of Applied Biology and Chemical Technology, The Hong Kong Polytechnic University, Hong Kong 999077, China
[11]Medical 3D Printing Center, Orthopedic Institute, Department of Orthopedic Surgery, The First Affiliated Hospital MOE Key Laboratory of Geriatric Diseases and Immunology, School of Biology and Basic Medical Sciences, Suzhou Medical College, Soochow University, Suzhou 215000, China
[12]Lead contact
*Correspondence: liuxiangmei@hebut.edu.cn (X.L.), slwu@pku.edu.cn (S.W.), xyliu@mail.sic.ac.cn (X.L.), wkkyeung@hku.hk (K.W.K.Y.)
https://doi.org/10.1016/j.celbio.2025.100213

THE BIGGER PICTURE Implant-associated infections and poor bone integration are major obstacles to the long-term success of orthopedic implants. Conventional antibacterial coatings often depend on exogenous agents or complex modifications, limiting their stability and clinical applicability. Here, we present a hydrogenated titanium dioxide (TiO_2) nanoscale honeycomb surface pattern (H-NCs) engineered onto titanium (Ti) implants. By introducing oxygen vacancies into the TiO_2 surface pattern, this design integrates near-infrared (NIR)-responsive antibacterial activity with immune-modulatory topography, enabling rapid, on-demand biofilm elimination and enhanced osteogenesis. Leveraging intrinsic material properties, this agent-free approach overcomes the limitations of traditional methods. The H-NCs surface thus offers an effective and clinically relevant strategy for overcoming infection and bone integration barriers in orthopedic implant applications.

SUMMARY

Post-implantation infections significantly threaten clinical outcomes due to limitations in traditional antibiotic therapies and challenges in meeting the complex requirements for both bacterial eradication and osteoimmunomodulation. Current approaches rarely eliminate biofilms and enhance osseointegration without complex additional components. Herein, we developed a hydrogenated titanium dioxide (TiO_2) nanoscale honeycomb surface pattern (H-NCs) by leveraging the inherent TiO_2 component on titanium (Ti) surfaces. These engineered H-NCs with oxygen vacancies narrowed the TiO_2 band gap to 1.32 eV, facilitating generation of reactive oxygen species (ROS) and mild hyperthermia for biofilm elimination under near-infrared (NIR) light. *In vitro* and *in vivo* results demonstrated rapid elimination of 99.94% and 91.58% of *Staphylococcus aureus* (*S. aureus*) within 15 min of NIR irradiation, respectively. Moreover, the 90-nm honeycomb-like surface structure directs macrophages by topographical cues, establishing a favorable osteoimmune microenvironment.

Please cite this article in press as: Zhu et al., NIR-responsive hydrogenated TiO_2 nanoscale honeycomb surface pattern for rapid *S. aureus* biofilm elimination and enhanced osteogenesis, Cell Biomaterials (2025), https://doi.org/10.1016/j.celbio.2025.100213

CellPress
OPEN ACCESS

Cell Biomaterials
Article

In general, this novel modified surface may address the challenges of implant-related infection and enhancing osteogenesis simultaneously.

INTRODUCTION

As the global population ages and trauma incidents rise, the demand for orthopedic procedures is increasing. For example, in the United States alone, over 2.8 million joint replacement surgeries, such as hip and knee operations are performed annually, with a growth rate exceeding 10% each year.[1–3] Despite strict adherence to aseptic procedures and prophylactic antibiotic interventions, implant-associated infections continue to pose a significant threat. In fact, these infections are not uncommon, as their rates can potentially exceed 30% in cases involving complex open fractures and revision surgeries.[4–6] Although antibiotics can be partially effective in preventing and managing infections, their usage in high doses and systemic exposure could lead to severe side effects.[6–9] Furthermore, the risk of reinfections persists after discontinuing the use of antibiotics.[10] For example, postoperative recurrent infections can last for over 5 years following implantation, presenting a reinfection risk of over 10%.[11]

Once pathogenic bacteria colonize the implant surface and form biofilms, it becomes challenging for the immune system and antibiotic treatments to eradicate them. For decades, addressing implant-associated infections has relied on a combination of invasive surgical procedures (such as one- or two-stage reimplantation) and long-term systemic antibiotic treatments.[12–14] These approaches often result in a prolonged recovery time, substantial healthcare costs, and the potential of life-long functional impairment for patients. What is worse, the rapid evolution of multidrug-resistant bacteria presents an escalating challenge to traditional antibiotic-based treatment methods.[15,16] Moreover, postoperative bacterial infections often accompany chronic inflammation and delayed bone-to-implant integration, thereby compromising the overall success of implantation surgeries. This highlights the increasing need for developing non-invasive and effective strategies to eliminate biofilm infections on implant surfaces and regulate osteoimmune responses to enhance bone-to-implant integration.

To address this issue, one potential solution lies in the development of *in situ* functional implant surfaces. For decades, researchers have been working on developing implant surface coatings to carry antibacterial agents such as antibiotics,[17] metal ions (e.g., silver, zinc, and copper ions),[18–20] antimicrobial peptides,[21,22] and other components.[23–25] These surface modification strategies aim to prevent bacterial adhesion, eliminate bacteria, and, in some cases, achieve a balance between their antibacterial capability and promotion of bone regeneration.[24,26] However, these coatings possess several limitations: (1) their capacity to carry antibacterial or bioactive agents is limited; (2) their antibacterial efficiency and potential toxicity to normal cells depend on the release of the incorporated agents, and managing this release in complex *in vivo* physiological environments remains challenging; (3) the coating will inevitably fail as the loaded agents are released or degraded. When the coating's effectiveness fades, reinfection may still occur over time. Once biofilms develop, repeated surgery and costly treatments become unavoidable.

Exogenous stimulus-responsive antibacterial surfaces have attracted considerable interest in research due to their high antibacterial efficiency and *in situ* controllability. For instance, photodynamic therapy (PDT) is an exogenous stimulus-responsive antibacterial technique that utilizes reactive oxygen species (ROS) generated by photo-responsive materials under light as the primary bactericidal agents.[27,28] Moreover, ROS toxicity to mammalian cells is minimal if exposure is temporary, as previously reported.[29] However, the development of photo-responsive surfaces generally necessitates the incorporation of additional constituents, such as photosensitizers or complex components.[28–31] This means the transition from research environments to clinical applications often faces challenges due to stability concerns and the extensive approval process necessary for translation.

To overcome these limitations, we focused on titanium dioxide (TiO_2), the native passivation layer that spontaneously forms on titanium (Ti) implants. Ti is widely used in dental and orthopedic applications due to its biocompatibility and mechanical strength. The intrinsic TiO_2 layer on Ti implants not only ensures biocompatibility but also exhibits photocatalytic properties.[32] However, the spontaneously formed TiO_2 layer has limited therapeutic utility due to its band gap (Eg) (3.0–3.2 eV) and rapid electron-hole recombination, which restrict its light absorption to the ultraviolet (UV) region.[33] This limitation restricts its application in the biomedical field due to the poor penetration power of UV light into the deep layers of human tissues.[34] In this study, we engineered a hydrogenated TiO_2 nanoscale honeycomb surface pattern (H-NCs) via high-temperature hydrogenation. This process introduced oxygen vacancies, narrowing the Eg and shifting the light absorption spectrum of TiO_2 into the near-infrared (NIR) window.[35–37] Unlike previously reported approaches that require complex additional components, our strategy enables NIR-activated antibacterial effects while preserving the TiO_2 honeycomb-like surface structures. This enhancement allows the surface to exhibit exceptional photo-responsive antibacterial properties without altering the intrinsic surface components of clinically used Ti implants.

Apart from the eradication of bacterial infection, a proper immune response at the bone-implant interface is crucial for determining the success of bone-to-implant integration. Building on our previous findings that the TiO_2 nanoscale honeycomb surface pattern (NCs) can modulate immune responses and promote bone-to-implant integration,[38,39] we specifically designed the proposed H-NCs to address both bacterial infection and osseointegration challenges simultaneously. Upon NIR irradiation, the tailor-made H-NCs generate substantial ROS and mild hyperthermia via oxygen-vacancy-enriched TiO_2, effectively eliminating implant-associated bacterial infections. Moreover, the preserved honeycomb-like surface structure exhibits superior osteoimmune modulation capability, thereby promoting bone-to-implant integration (Scheme 1). In summary, this

Please cite this article in press as: Zhu et al., NIR-responsive hydrogenated TiO_2 nanoscale honeycomb surface pattern for rapid *S. aureus* biofilm elimination and enhanced osteogenesis, Cell Biomaterials (2025), https://doi.org/10.1016/j.celbio.2025.100213

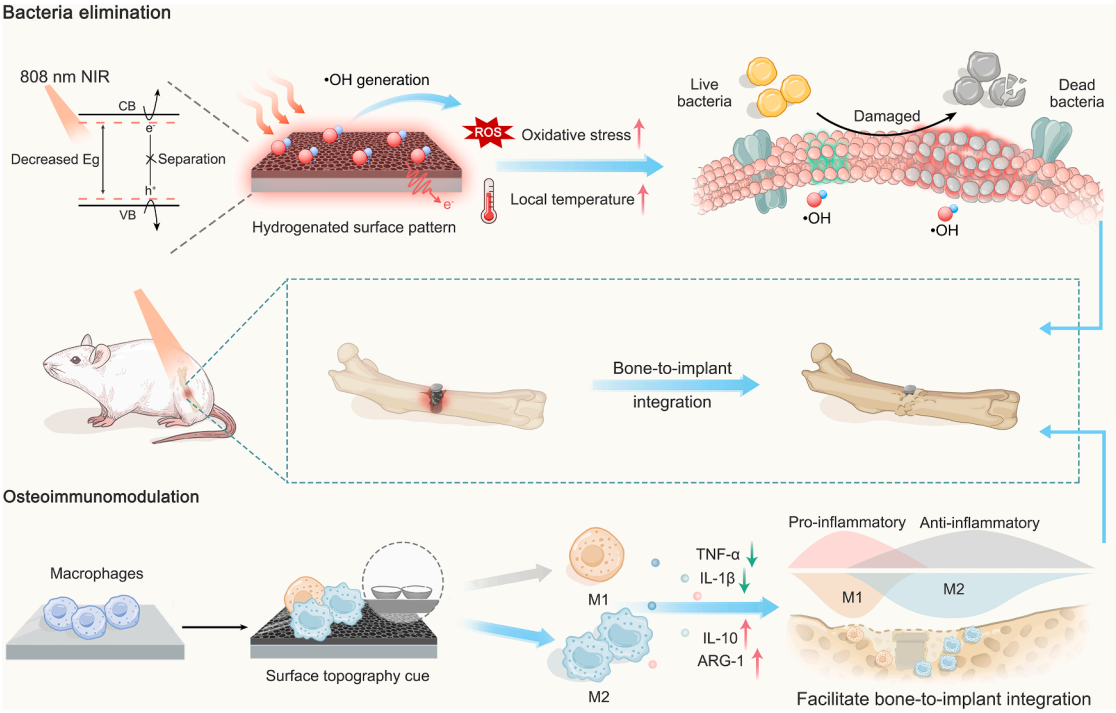

Scheme 1. Schematic illustration of H-NCs on Ti implants, enabling NIR-activated antibacterial effects via enhanced ·OH generation and mild hyperthermia, and promoting bone-to-implant integration through immunomodulatory surface topography.

agent-free, structure-based strategy overcomes the limitations of existing surface modifications by concurrently achieving controllable, NIR-driven antibacterial performance and immunomodulatory effects through a simple and translatable process.

RESULTS AND DISCUSSION

Synthesis and characterization of H-NCs

As illustrated in Figure 1A, NCs were first established on the Ti implant surface using a customized method that employed polystyrene spheres as sacrificial templates.[39] Following this, the NCs underwent hydrogen plasma treatment to generate oxygen vacancies on the surface, resulting in H-NCs. The photographs in Figure 1B reveal a color change from a blue NCs surface to a black H-NCs surface. In comparison to polished Ti surfaces, a unique honeycomb-like surface structure was observed on the NCs surface, which remained intact after the hydrogenation process on the H-NCs surface. Atomic force microscopy (AFM) confirmed comparable surface roughness among polished Ti, NCs, and H-NCs (Table S1). The structure of NCs and H-NCs on Ti surfaces was further investigated using high-resolution transmission electron microscopy (HR-TEM). As shown in Figure 1C, the lattice spacings of 3.43 Å in NCs closely match to the lattice spacing of the (101) planes of anatase TiO_2.[40] Notably, curved lattices were observed in H-NCs, suggesting the presence of lattice defects.[41]

The crystalline structure of the samples was characterized by X-ray diffraction (XRD). As shown in Figure 1D, NCs and H-NCs show identical diffraction peaks of anatase TiO_2. The surface elements of the different samples were further analyzed using X-ray photoelectron spectroscopy (XPS). Beyond the consistent detection of Ti and O, no additional elements were identified in both NCs and H-NCs (Figure 1E). As shown in Figure 1F, the high-resolution Ti 2p spectra of polished Ti surfaces and NCs exhibited two peaks at 459.1 and 464.9 eV, corresponding to Ti^{4+}.[42] However, these peaks shifted toward lower binding energies in the H-NCs spectra, indicating a higher electron density in H-NCs.[43] Neither NCs nor H-NCs showed obvious Ti^{3+} peaks, suggesting that the amount of Ti^{3+} was very low in both samples. Furthermore, the deconvolution of the O 1s peak indicated that the ratio of the percentage of defective oxygen in H-NCs was 32.65%,[44] which was much higher than that of Ti^{3+} content, suggesting the oxygen vacancies were the main defects (Figure 1G). In addition, electron paramagnetic resonance (EPR) was employed to examine oxygen vacancy and Ti^{3+} across the samples. As shown in Figure 1H, no signs of Ti^{3+} were detected, while H-NCs exhibited an oxygen vacancy related signal at g = 2.003,[41] which corresponds with the results of XPS. These results indicate that hydrogenation successfully introduced oxygen vacancies on the surface of H-NCs.

Photocatalytic and photothermal performance of H-NCs

The generation of ROS in different samples was first investigated using dichlorofluorescein diacetate (DCFH-DA), which captures ROS and produces 2′,7′-dichlorofluorescein (DCF) fluorescence. As shown in Figure 2A, no ROS were detected in any samples without NIR irradiation. After 15 min of NIR irradiation, NCs generated only a negligible amount of ROS. In comparison,

Please cite this article in press as: Zhu et al., NIR-responsive hydrogenated TiO_2 nanoscale honeycomb surface pattern for rapid *S. aureus* biofilm elimination and enhanced osteogenesis, Cell Biomaterials (2025), https://doi.org/10.1016/j.celbio.2025.100213

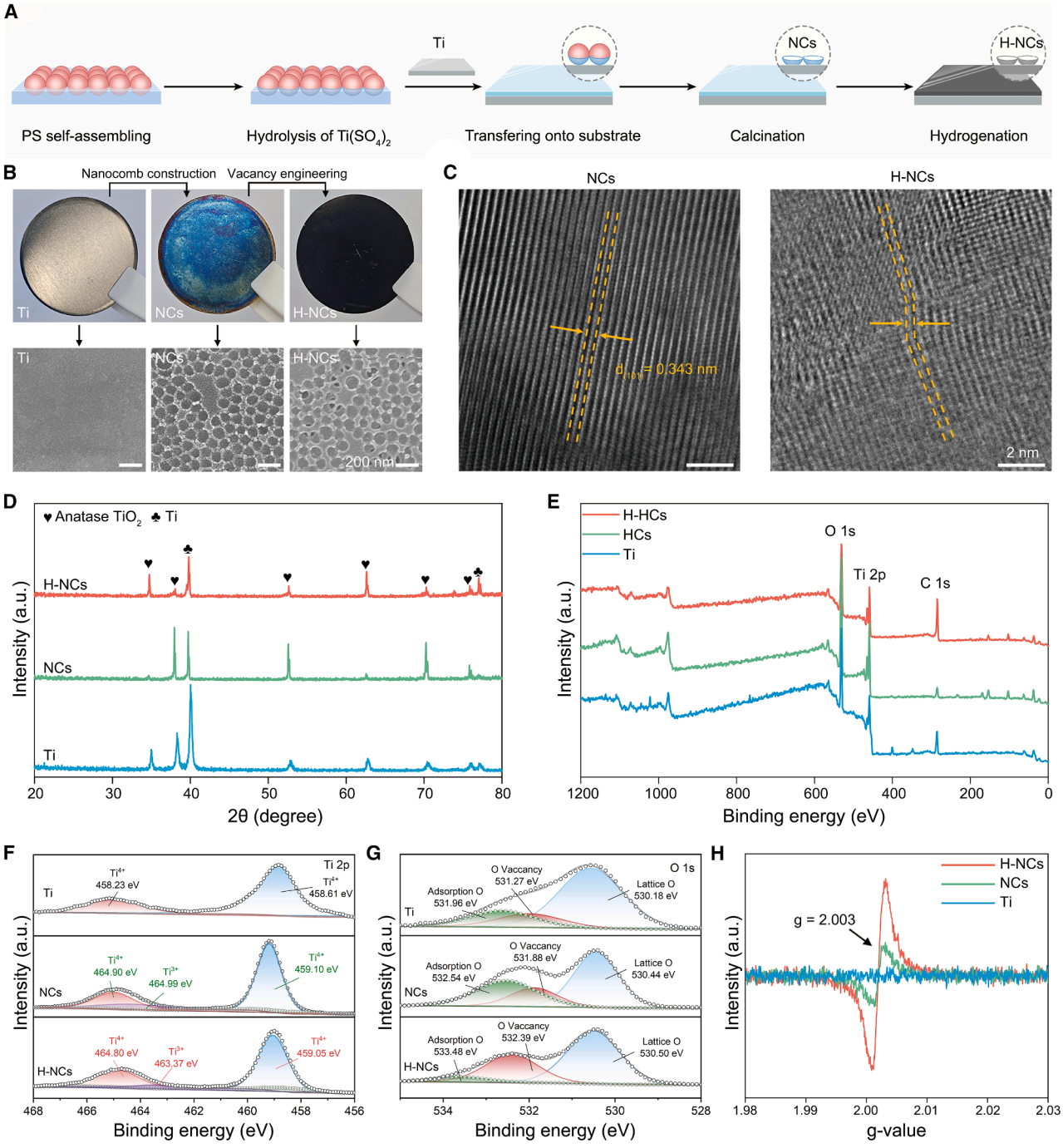

Figure 1. Surface characterizations of different samples

(A) Schematic illustration of the H-NCs preparation process using polystyrene spheres as sacrificial templates, followed by hydrogen plasma treatment.
(B) Representative photographs and SEM images of samples. Scale bar in SEM images, 200 nm.
(C) Representative HR-TEM images of NCs and H-NCs. Scale bar, 2 nm.
(D) XRD patterns of Ti, NCs, and H-NCs.
(E) XPS survey spectra from 200 to 1,200 eV for Ti, NCs, and H-NCs.
(F) Ti 2p spectra of Ti, NCs, and H-NCs.
(G) O 1s spectra of Ti, NCs, and H-NCs.
(H) EPR spectra of Ti, NCs, and H-NCs.

Please cite this article in press as: Zhu et al., NIR-responsive hydrogenated TiO_2 nanoscale honeycomb surface pattern for rapid *S. aureus* biofilm elimination and enhanced osteogenesis, Cell Biomaterials (2025), https://doi.org/10.1016/j.celbio.2025.100213

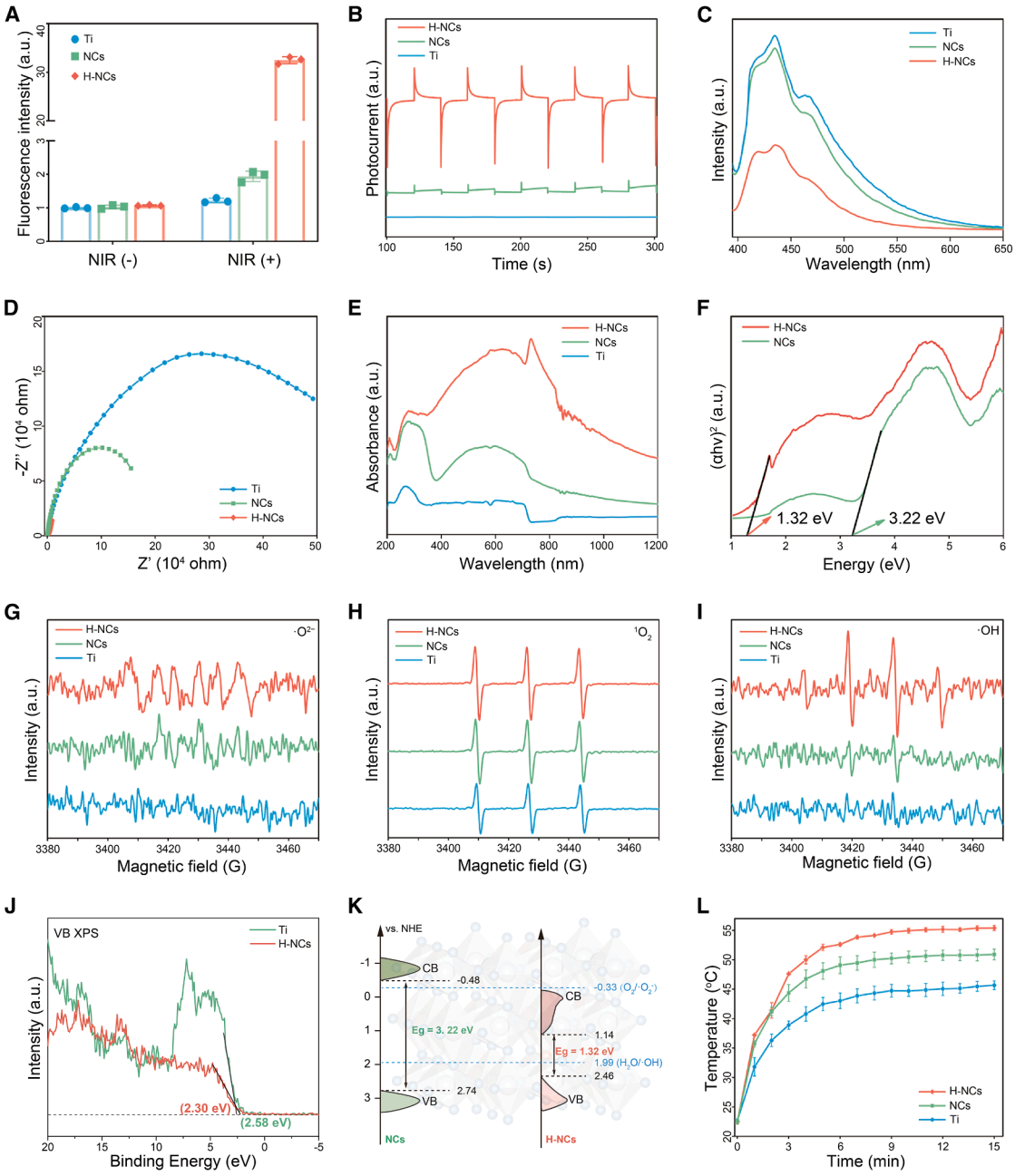

Figure 2. Photocatalytic and photothermal performance of different samples

(A) ROS generation detected by DCFH-DA assay (n = 3).
(B) Photocurrent generation of Ti, NCs, and H-NCs under NIR irradiation.
(C) PL spectra of Ti, NCs, and H-NCs
(D) EIS curves of Ti, NCs, and H-NCs.
(E) UV-vis-NIR DRS of Ti, NCs, and H-NCs.
(F) Corresponding Tauc plots derived from the UV-vis-NIR spectra.
(G) ESR spectra of superoxide radical ($\cdot O^{2-}$) generated by Ti, NCs, and H-NCs after 15 min NIR irradiation.
(H) ESR spectra of singlet oxygen ($^1O_2$) generated by Ti, NCs, and H-NCs after 15 min NIR irradiation.
(I) ESR spectra of hydroxyl radical (·OH) generated by Ti, NCs, and H-NCs after 15 min NIR irradiation.
(J) Valence band XPS spectra of NCs and H-NCs.
(K) Schematic illustration comparing the DOSs of H-NCs and NCs.
(L) Temperature changes of Ti, NCs, and H-NCs after 15 min NIR irradiation (n = 3). Data are presented as mean ± SD.

Please cite this article in press as: Zhu et al., NIR-responsive hydrogenated TiO_2 nanoscale honeycomb surface pattern for rapid *S. aureus* biofilm elimination and enhanced osteogenesis, Cell Biomaterials (2025), https://doi.org/10.1016/j.celbio.2025.100213

H-NCs demonstrated superior photocatalytic performance, producing a significantly higher amount of ROS. Figure 2B shows photocurrent densities of different samples under NIR irradiation. Compared with polished Ti and NCs, H-NCs exhibited a stronger photocurrent density, indicating an enhanced spatial charge separation ability.[45] This result was further confirmed by photoluminescence (PL) spectra (Figure 2C). The quenched characteristic peaks of H-NCs suggest the lowest radiative recombination rate of photogenerated electron-hole pairs and a longer electron lifetime.[46] The efficient carrier transfer was further evidenced by the reduction in the photocarrier transfer barrier of H-NCs, as indicated by the electrochemical impedance spectroscopy (EIS) results (Figure 2D). Among all samples, H-NCs exhibited the lowest impedance, indicating that the H-NCs could reduce electrochemical impedance and consequently promote charge transfer.[47]

To investigate the photocatalytic performance of H-NCs based on its Eg, the light absorption capabilities of different samples were assessed using UV-vis-NIR diffuse reflectance spectra (DRS). As shown in Figure 2E, H-NCs exhibited a substantial enhancement in absorbance compared with polished Ti surfaces and NCs from 200 to 1,200 nm, which can be attributed to the increased oxygen deficiency.[48] Based on the DRS results, Tauc plots were generated to measure the Eg of NCs and H-NCs (Figure 2F). The Eg of NCs was calculated to be approximately 3.22 eV, slightly greater than that of bulk anatase TiO_2. In comparison, the calculated Eg of H-NCs was reduced to 1.32 eV, which was below the energy level of 808-nm NIR photons (1.53 eV).[49] This allowed H-NCs to undergo electron transitions and subsequently generate photoelectron-hole pairs upon exposure to 808-nm NIR radiation. The color transformation from blue on NCs to black on H-NCs can be attributed to the presence of oxygen vacancies,[50] which reduced the Eg and contributed to the expansion of the light absorption range. The stability of the H-NCs surface was demonstrated by observing no color changes in the H-NCs over a period of 1 year after preparation.

Next, electron spin resonance (ESR) spectra were used to measure the types of ROS generated by different samples under NIR irradiation. Three major ROS, including superoxide radical ($\cdot O^{2-}$), singlet oxygen ($^1O_2$), and hydroxyl radical (·OH), were measured. As shown in Figures 2G and S1A, no significant difference was detected in the $\cdot O^{2-}$ signal among different samples. Although a slight increase in the $^1O_2$ signal at different time points (Figure S1B) was observed, the difference between the three groups after 15 min of NIR irradiation became insignificant (Figure 2H). In contrast, an intensified ·OH signal was detected in H-NCs under 808-nm NIR irradiation throughout different measuring time points (Figures 2I and S1C). These results indicate that ·OH was the primary generated ROS by H-NCs under 808-nm NIR irradiation.

To further understand the underlying mechanism of ROS generation, the density of states (DOSs) of the valence band maximum (VBM) of NCs and H-NCs were measured using VB-XPS (Figure 2J). The typical valence band DOS characteristics of TiO_2 were observed on NCs, with the edge of the maximum energy at about 2.58 eV (vs. vacuum). Thus, the VBM of NCs could be calculated to be 2.74 eV (vs. NHE) according to the formula E_{VB} (vs. NHE) = φ + E_{VB} (VB-XPS) − 4.44, where φ is the work function of the instrument (4.6 eV).[51] The Eg of NCs is 3.22 eV, as calculated by the Tauc plots, thus the conduction band minimum (CBM) would be at about −0.48 eV. As shown in Figure 2J, the VBM of H-NCs energy blue-shifts toward the vacuum level at approximately 2.30 eV. Thus, the VBM (vs. NHE) could be calculated to be 2.46 eV. According to the Tauc plots result, the Eg of H-NCs is 1.32 eV, resulting in a calculated CBM of H-NCs of approximately 1.14 eV.

Figure 2K illustrated the ROS generation mechanism under 808-nm NIR irradiation. The presence of oxygen vacancies leads to an extended tail and narrows the Eg of H-NCs,[52] which was calculated to be 1.32 eV (Figure 2F). This narrowed Eg (<1.53 eV) allows electrons to be excited from the VB to the CB under 808-nm NIR irradiation.[49] The oxygen vacancies in anatase TiO_2 can act as trap sites for photogenerated electrons, promoting the separation of electron-hole pairs. This enhanced charge separation may lead to a higher concentration of holes in the valence band, which can then participate in the oxidation of H_2O or OH^- to produce ·OH radicals.

An increase in local temperature can affect the functionality of proteins and membrane permeability in bacteria, impacting their metabolism.[28,53,54] The enhanced light absorption of H-NCs not only facilitated ROS generation but also elevated the surface temperature within 15 min upon irradiation under NIR (Figures 2L and S2A). H-NCs exhibited the best photothermal performance compared with other samples, with the final temperature reaching 55.4°C (Figure S2B). The consistent heating/cooling curves indicated that H-NCs exhibited exceptional photothermal stability, with no significant temperature change observed after multiple irradiation cycles (Figure S2C).

As summarized in Table S2, compared with NCs, H-NCs preserve the honeycomb-like surface structure while exhibiting efficient NIR responsiveness. Defect engineering endows H-NCs with significantly enhanced ROS generation and photothermal effects under 808-nm irradiation, without compromising their unique surface topography.

In vitro antibacterial performance

The spread plate method was used to investigate the antibacterial performance of different samples against *Staphylococcus aureus* (*S. aureus*) (Figure S3). *S. aureus* on the polished Ti surface, NCs, and H-NCs were subjected to either 15 min of NIR irradiation (indicated by -NIR(+) following the sample names) or no NIR treatment (indicated by -NIR(−) following the sample names). Subsequently, *S. aureus* treated on different samples were diluted and spread on agar plates. None of the samples exhibited significant antibacterial performance without NIR irradiation. After 15 min of NIR irradiation, a slight increase in the antibacterial ratio was observed in the Ti-NIR(+) and NCs-NIR(+) groups, with 24.53% and 29.47% respectively, compared with the Ti-NIR(−) as the control group (Figure 3A). The limited suppression of *S. aureus* in the Ti-NIR(+) and NCs-NIR(+) groups could be attributed to the weak photothermal effect, which had a minor impact on the viability of *S. aureus*.[28,54] However, the mild heat alone was insufficient to effectively eliminate *S. aureus*. In comparison, H-NCs combined effective ROS generation and an enhanced photothermal effect, leading to a rapid

Please cite this article in press as: Zhu et al., NIR-responsive hydrogenated TiO_2 nanoscale honeycomb surface pattern for rapid *S. aureus* biofilm elimination and enhanced osteogenesis, Cell Biomaterials (2025), https://doi.org/10.1016/j.celbio.2025.100213

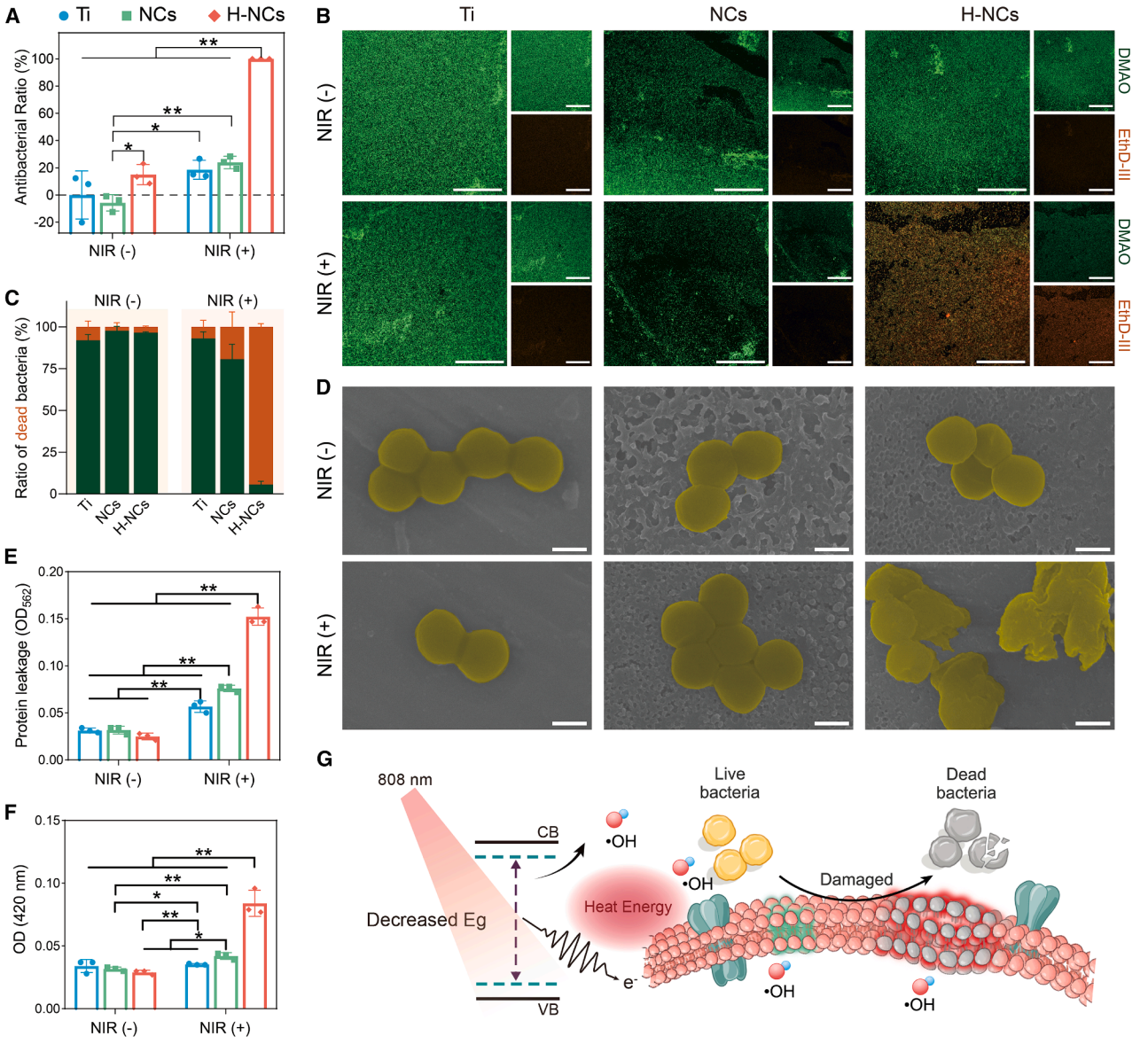

Figure 3. *In vitro* antibacterial evaluation

(A) Antibacterial ratio of Ti, NCs, and H-NCs against *S. aureus* without NIR irradiation and after 15 min of NIR irradiation.
(B) Live/dead fluorescence staining images of *S. aureus* on different samples. Scale bars, 200 μm.
(C) Semi-quantitative analysis of the dead bacteria ratio from live/dead staining images.
(D) SEM images of *S. aureus* on different samples. Scale bars, 500 nm.
(E) Protein leakage from *S. aureus* detected by BCA assay after treatment with different samples.
(F) ONPG hydrolysis indicating membrane permeability changes in *S. aureus* after treatment.
(G) Schematic illustration of the antibacterial mechanism. $n = 3$ independent experiments per group, $^{*}p < 0.05$ and $^{**}p < 0.01$. Data are presented as mean ± SD.

elimination of bacteria and achieving an impressive antibacterial ratio of 99.94% within 15 min of NIR irradiation.

To further investigate *in vitro* antibacterial performance, live/dead fluorescent staining was conducted using two fluorescent dyes, N, N-dimethylaniline N-oxide (DMAO) and Ethidium Homodimer III (EthD-III) (Figures 3B and 3C). DMAO is a green nucleic acid fluorescent dye that stains both live and dead bacteria, whereas EthD-III is a red nucleic acid fluorescent dye that stains only dead bacteria with damaged cell membranes. *S. aureus* survival rates were consistent across all groups, except for H-NCs-NIR(+), which aligned with the spread plate count results.

In order to explore the antibacterial mechanism of H-NCs under NIR irradiation, evaluation of changes in bacterial morphology, protein leakage, and the permeability of the cytoplasmic membrane were performed (Figure 3D). *S. aureus* exhibited typical spherical shapes, smooth surfaces, and distinct

Please cite this article in press as: Zhu et al., NIR-responsive hydrogenated TiO_2 nanoscale honeycomb surface pattern for rapid *S. aureus* biofilm elimination and enhanced osteogenesis, Cell Biomaterials (2025), https://doi.org/10.1016/j.celbio.2025.100213

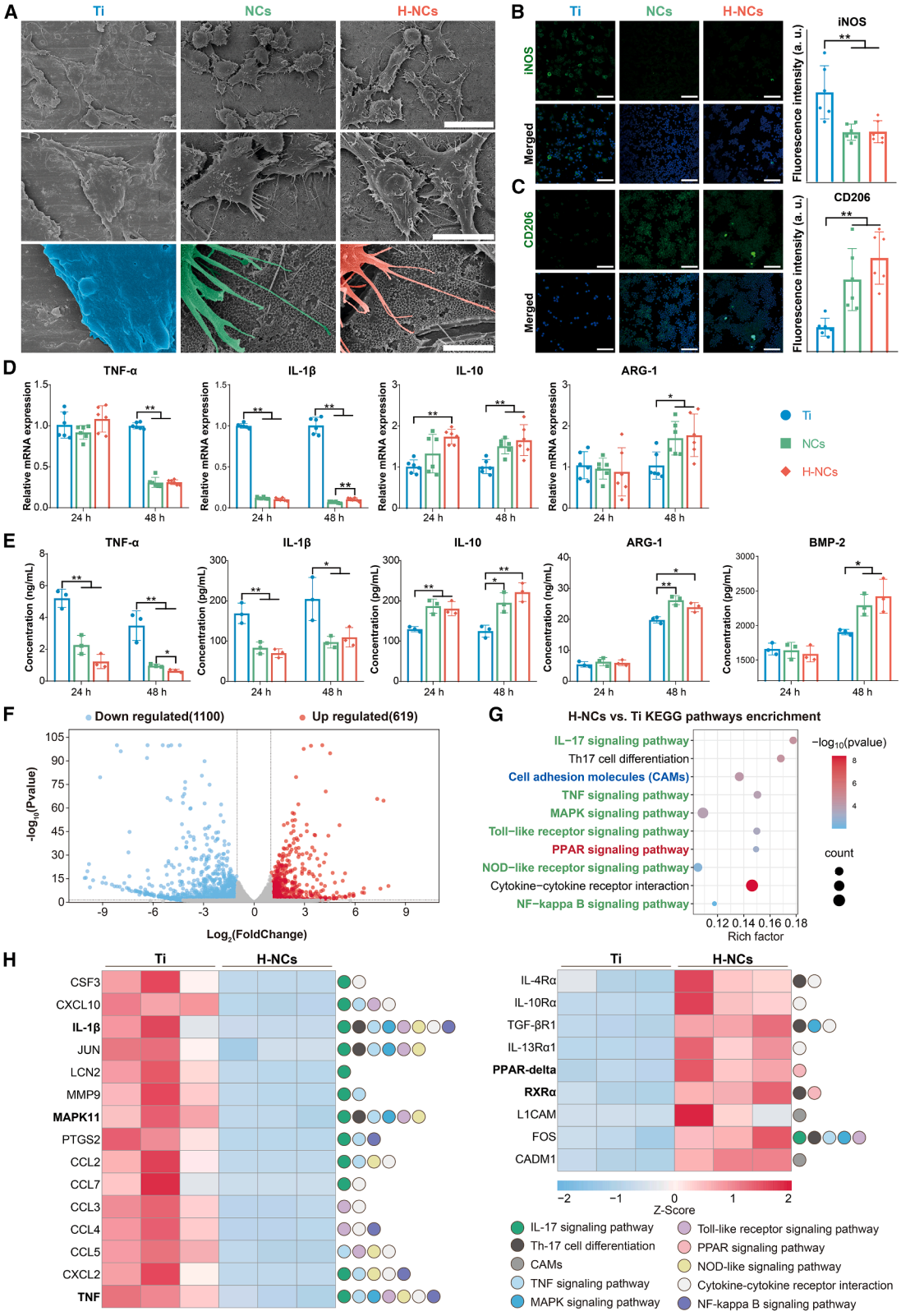

(legend on next page)

Please cite this article in press as: Zhu et al., NIR-responsive hydrogenated TiO_2 nanoscale honeycomb surface pattern for rapid *S. aureus* biofilm elimination and enhanced osteogenesis, Cell Biomaterials (2025), https://doi.org/10.1016/j.celbio.2025.100213

boundaries on Ti-NIR(−). The morphologies of bacteria remained intact on both Ti and NCs surfaces, even after NIR treatment. In contrast, *S. aureus* on H-NCs-NIR(+) showed abnormal morphologies, characterized by loss of membrane integrity and wrinkled shapes, indicating bacterial death.[55,56] The protein leakage from *S. aureus* on different samples following treatment with or without NIR irradiation was measured using a commercial bicinchoninic acid (BCA) assay kit (Figure 3E). The overall trend of results was consistent with the antibacterial findings. Protein leakage from *S. aureus* on all samples was negligible without NIR irradiation. Upon exposure to NIR, all samples showed a rise in protein leakage compared with their non-irradiated counterparts, with H-NCs exhibiting the most substantial protein leakage, exceeding 4.86 times that of the Ti-NIR(−) as the control group. The permeability of the *S. aureus* cell membrane was then assessed via ortho-nitrophenyl-β-galactoside (ONPG) hydrolysis (Figure 3F). The highest optical density (OD) at 420 nm for H-NCs-NIR(+) indicated that the cell membrane of *S. aureus* had been irreversibly damaged, consistent with the bacterial morphology observed using scanning electron microscopy (SEM).

In summary, H-NCs exhibited outstanding antibacterial effectiveness *in vitro* when subjected to NIR irradiation within a short duration of 15 min. Figure 3G demonstrates the antibacterial mechanism in which H-NCs rapidly generate both heat and a substantial amount of ROS upon NIR irradiation. The photothermal effect undermines the bacterial cytoplasmic membrane's structural integrity, leading to increased membrane permeability. This enabled ROS to infiltrate and impair bacterial enzymes and proteins. As a result, the sufficient ROS generated by H-NCs effectively eradicated the bacteria, causing the release of bacterial contents and ultimately leading to the rapid elimination of the bacteria.

In vitro regulation on macrophages

After confirming the antibacterial capability of H-NCs, we proceeded to examine their immunomodulatory role in regulating a widely used murine macrophage cell line (RAW 264.7). The influence of NIR irradiation on cells cultured on different samples was first evaluated (Figure S4). The 15-min NIR exposure showed no significant effect on macrophages, allowing us to focus on substrate-driven effects. Cell morphologies on different samples were observed using SEM. As shown in Figure 4A, abundant filopodia were observed in macrophages cultured on NCs, in contrast to the smooth boundary observed on the Ti surface. A similar cell morphology with abundant and stretching filopodia was also found on H-NCs, suggesting that the hydrogenation process did not influence the modulatory role of the honeycomb-like surface structures on macrophage morphologies. Subsequently, we stained macrophages on different samples with an M1 macrophage marker inducible nitric oxide synthase (iNOS) and an M2 macrophage surface marker (CD206). As shown in Figures 4B and 4C, NCs and H-NCs exhibited similar downregulation of iNOS and upregulation of CD206.

Macrophages are essential in the bone-to-implant integration process. For instance, an early inflammatory phase marked by the temporary presence of tumor necrosis factor-alpha (TNF-α) can trigger the regeneration process and facilitate the recruitment of mesenchymal stem cells (MSCs), which play a crucial role in bone regeneration.[57,58] However, it is important to note that prolonged inflammation dominated by M1 macrophages, characterized by high levels of pro-inflammatory cytokines such as TNF-α and interleukin-1 beta (IL-1β), can lead to chronic inflammation, fibrous capsule formation, bone resorption, and even implant failure.[58,59] A reduced inflammatory response and timely switching of macrophages from M1 to M2 phenotype is considered more favorable during the later stage of the regeneration process.[59,60] Therefore, a properly mediated osteoimmune microenvironment is vital for successful bone-to-implant integration.[39,61,62] We next explored the relationship between culturing time and macrophage polarization on different samples using real-time qPCR (Figure 4D) and ELISA (Figure 4E) after culturing macrophages on various surfaces for 24 and 48 h, respectively. The 24-h results revealed that despite no significant difference in TNF-α expression levels between NCs and H-NCs, the secretion levels of both TNF-α and IL-1β were suppressed. The pro-inflammatory response remained inhibited at 48 h, as indicated by both real-time qPCR and ELISA results. Similarly, no difference was observed in arginase-1 (ARG-1) at 24 h, but ARG-1 was upregulated alongside interleukin-10 (IL-10) later at 48 h. The overall pattern of these results aligned with the aforementioned fluorescent staining at 48 h, suggesting that the honeycomb-like surface structure of both NCs and H-NCs can suppress M1 macrophages while promoting M2 macrophage polarization after 48 h of culturing. Furthermore, bone morphogenetic protein-2 (BMP-2), a potent osteogenic inducer secreted by macrophages,[63] showed comparable secretion levels between NCs and H-NCs at 24 h but was significantly upregulated in both groups at 48 h. This delayed BMP-2 elevation coincided temporally with the M1-to-M2 phenotypic shift observed at 48 h, suggesting that the honeycomb-like topography orchestrates macrophage-mediated osteoimmunomodulation. By 48 h, the transition to M2 dominance established a regenerative microenvironment characterized by synergistic secretion of BMP-2,

Figure 4. Regulation on macrophages by H-NCs

(A) Representative morphologies of macrophages on different samples. Scale bars, 20 μm (first row), 10 μm (second row), and 2 μm (third row).
(B) Fluorescence staining images of iNOS in macrophages on different samples, and corresponding quantification of fluorescence intensity. Scale bar, 100 μm.
(C) Fluorescence staining images of CD206 in macrophages on different samples, and corresponding quantification of fluorescence intensity. Scale bar, 100 μm.
(D) Relative mRNA expression levels of M1 macrophage-related genes (TNF-α and IL-1β) and M2 macrophage-related genes (IL-10 and ARG-1) at 24 and 48 h.
(E) ELISA results of pro-inflammatory cytokines (TNF-α and IL-1β), anti-inflammatory cytokines (IL-10 and ARG-1), and pro-osteogenic cytokine (BMP-2) at 24 and 48 h.
(F) Volcano plot of differentially expressed genes in H-NCs compared with Ti.
(G) Enriched KEGG pathways identified in H-NCs compared with Ti.
(H) Differentially expressed genes contributing to KEGG pathway enrichment analysis. $n \geq 3$ independent experiments per group, $^{*}p < 0.05$ and $^{**}p < 0.01$. Data are presented as mean ± SD.

Please cite this article in press as: Zhu et al., NIR-responsive hydrogenated TiO_2 nanoscale honeycomb surface pattern for rapid *S. aureus* biofilm elimination and enhanced osteogenesis, Cell Biomaterials (2025), https://doi.org/10.1016/j.celbio.2025.100213

IL-10, and ARG-1—a cytokine profile known to promote bone regeneration while resolving inflammation.[64–66] This temporal regulation balances early inflammatory signals required to initiate the regeneration process with the later M2-driven secretion of pro-regenerative factors, thereby fostering a favorable osteoimmune environment for osteogenesis.

These findings, consistent with our previous study,[39] revealed that macrophage behaviors, including cell morphologies, M1/M2 gene expression level, and cytokine secretion profile, were indistinguishable between NCs and H-NCs. Although lattice perturbations and relaxation dynamics have been reported to influence cellular behavior,[67] the nearly identical surface morphology and roughness parameters between NCs and H-NCs indicate that macrophage polarization was governed by shared topographical cues rather than lattice-specific mechanical properties. This suggests that surface topography driven immunomodulatory mechanisms override subtle crystallographic variations in modulating the osteoimmune microenvironment.

The underlying mechanism of H-NCs' influence on macrophage regulation was further explored through transcriptomic analysis. Compared with the polished Ti surface, the volcano plots revealed that macrophages cultured on H-NCs displayed 619 upregulated and 1,100 downregulated genes (Figure 4F). These differentially expressed genes were collected and analyzed using the Kyoto Encyclopedia of Genes and Genomes (KEGG) to identify significantly enriched signaling pathways between H-NCs and Ti (Figure 4G). The differentially expressed genes contributing to these enriched KEGG pathways were further analyzed to generate heatmaps (Figures 4H and S5). Notably, several signaling pathways associated with M1 macrophage activation, including IL-17 signaling pathway, TNF signaling pathway, mitogen-activated protein kinase (MAPK) signaling pathway, Toll-like receptor signaling pathway, nucleotide-binding oligomerization domain (NOD)-like receptor signaling pathway, and nuclear factor (NF)-kappa B signaling pathways,[68–71] were downregulated. This downregulation was characterized by the decreased expression of genes typically associated with pro-inflammatory macrophage activation, such as IL-1β, MAPK11, and TNF.[69,72] Moreover, the downregulation of the M1-associated gene CD80 corresponds with the observed decrease in pro-inflammatory genes and cytokine secretion, such as TNF-α and IL-1β (Figures 4D and 4E). In contrast, upregulation of genes like peroxisome proliferator-activated receptor delta (PPAR-delta) and retinoid X receptor alpha (RXRα), which are involved in the activation of the PPAR signaling pathway, were observed and are known to be associated with M2 macrophage polarization.[73] Our findings suggest that the honeycomb-like surface pattern preserved by the hydrogenation process plays a crucial role in modulating macrophage behavior. This pattern not only suppresses M1 macrophage polarization but also promotes M2 macrophage polarization. Importantly, both the enriched cell adhesion molecules (CAMs) KEGG pathways and the heatmap of differentially expressed genes (Figure S5) confirm their crucial role as key mediators in mechanotransduction within this process. Specifically, L1 cell adhesion molecule (L1CAM) is associated with the RhoA/ROCK pathway, which is important for cytoskeletal remodeling and subsequent changes in cellular behavior.[74,75] This observation aligns with previous findings that a nanosized honeycomb-like topography induces cytoskeletal remodeling and M2 polarization, primarily through the modulation of the RhoA/ROCK signaling pathway.[39]

In vivo antibacterial activity

Given the outstanding antibacterial efficiency and immunomodulatory effect on macrophages of H-NCs observed *in vitro*, we proceeded to assess the anti-biofilm efficacy and bone-to-implant integration of H-NCs using an *S. aureus* biofilm-infected bone-implant model *in vivo*. To minimize the number of animals used, Ti-NIR(+) (serving as the control group) and H-NCs-NIR(+) were selected for the *in vivo* experiments. The animal experiment procedure is illustrated in Figure 5A, prior to implantation surgery, rod-shaped Ti and H-HC samples were first immersed in *S. aureus* suspension and subsequently cultured for 48 h to enable bacterial colonization on the implant surfaces and form biofilm (Figure S6). A 2-mm defect was created in the tibia plateau area using a hand drill, and the implants with pre-cultured *S. aureus* biofilm were inserted into the defects. 2 days after surgery, 15 min of NIR irradiation were applied to the surgical areas (Figure S7). In comparison to unmodified Ti, H-NCs still exhibited a photothermal response capability in the *in vivo* implantation model, and no tissue damage was seen after 15 min of NIR exposure on the sutured tissue.

To evaluate the *in vivo* antibacterial performance, part of the animal cohort was sacrificed and samples were pulled out and rolled on agar plates, followed by 24-h culturing. Figure 5B demonstrates a substantial presence of bacterial colonies in the Ti-NIR (+) group, in contrast to the sparse colonies in the H-NCs-NIR(+) group. The antibacterial ratio for H-NCs-NIR(+) was determined to be 91.58%, suggesting the effective elimination of the pre-existing *S. aureus* biofilm on the surface by H-NCs *in vivo*.

Photographs of the surgical sites for both groups were taken using a digital camera after 14 and 28 days (Figure 5C). On day 14, conspicuous secretions and pus were observed in the Ti-NIR(+) group, suggesting an intense inflammatory response in the tissue due to *S. aureus* infection. By the 28th day, the level of secretions had diminished, possibly due to the progression of the healing process over time. In contrast, observations on both days 14 and 28 showed no evidence of secretions or pus in the H-NCs-NIR(+) group, indicating the successful eradication of *S. aureus* and a decreased inflammatory response.[28] The Giemsa staining results are consistent with the observations in the photographs and the antibacterial evaluation results. As marked by red arrows, a substantial amount of bacteria was present in the Ti-NIR(+) group on day 14. By day 28, the bacterial count had reduced, but a notable quantity was still visible in the Ti-NIR(+) group. In contrast, the H-NCs-NIR(+) group showed hardly any detectable bacteria.

In addition to eliminating bacterial infection, an appropriate immune response at the bone-implant interface is crucial for the success of implant-to-bone integration. As shown in Figures 5D and 5E, the pan marker of macrophages (CD68) was positively expressed in both groups at both days 14 and 28, indicating the infiltration of immune cells to the implantation area. Although TNF-α-positive macrophages were present in both groups at both days 14 and 28, the surface structure of H-NCs demonstrated its capability to alleviate the inflammatory response, with fewer TNF-α but more IL-10 fractions. In summary, these results indicate

Please cite this article in press as: Zhu et al., NIR-responsive hydrogenated TiO_2 nanoscale honeycomb surface pattern for rapid *S. aureus* biofilm elimination and enhanced osteogenesis, Cell Biomaterials (2025), https://doi.org/10.1016/j.celbio.2025.100213

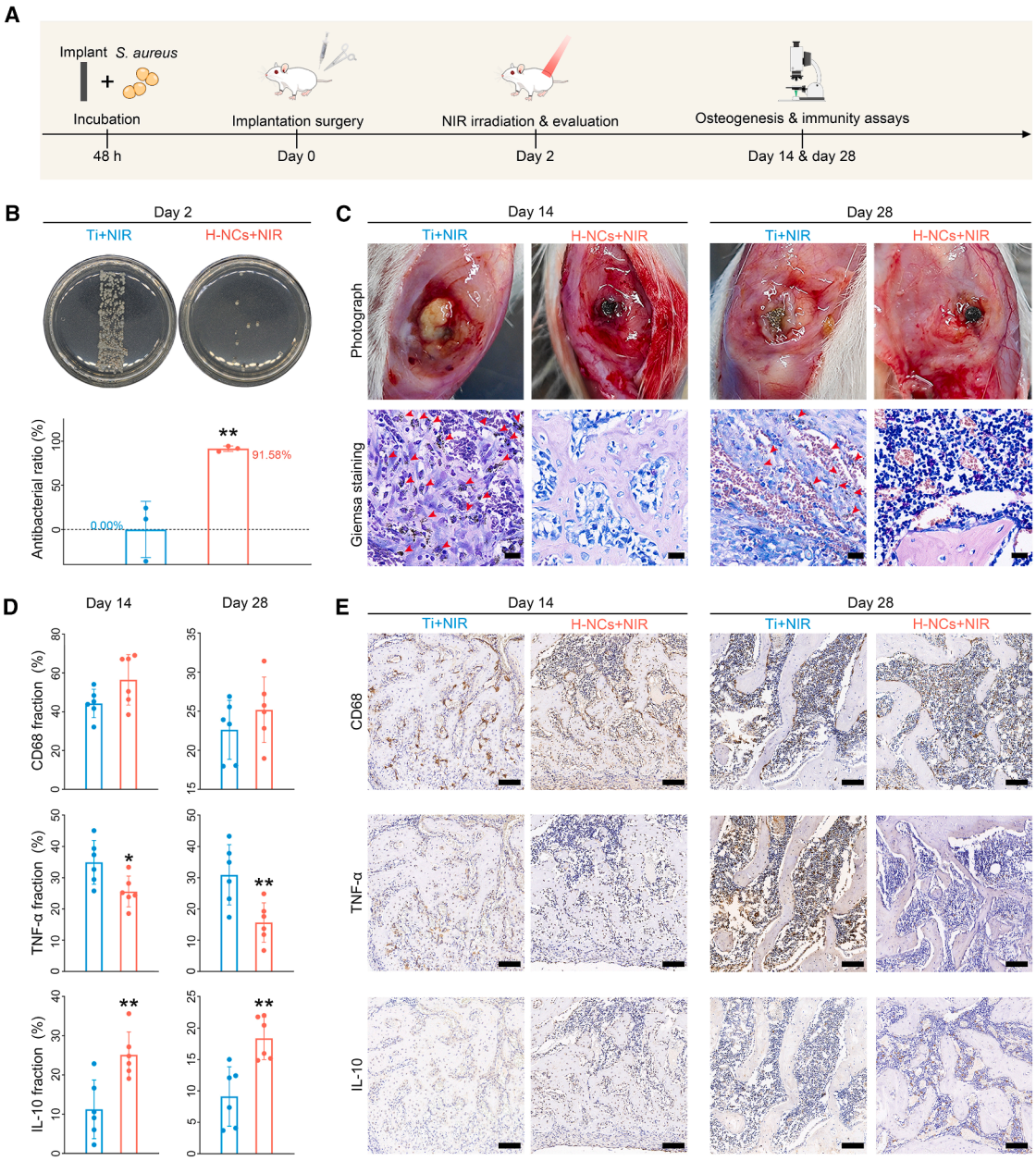

Figure 5. *In vivo* assessment of antibacterial and immune regulation on macrophages

(A) Schematic illustration of the *in vivo* study design.

(B) Remaining bacterial colonies on Ti and H-NCs rods extracted from bone tissue, and the corresponding calculated antibacterial ratio.

(C) Photographs of implant sites and Giemsa staining of bone tissue surrounding the implants (scale bar for Giemsa staining, 20 μm).

(D) Semi-quantitative analysis of positively stained cells in immunohistochemical images of CD68, TNF-α, and IL-10 at 14- and 28-days post-implantation.

(E) Representative immunohistochemical staining of CD68, TNF-α, and IL-10 in bone tissue around the implants at 14 and 28 days. Scale bars, 100 μm. $n \geq 3$ independent experiments per group, $^{*}p < 0.05$ and $^{**}p < 0.01$. Data are presented as mean ± SD.

that H-NCs can effectively eradicate *S. aureus* infection *in vivo* and reduce severe inflammatory responses.

Bone-to-implant integration *in vivo*

Further investigation was conducted into the bone-to-implant integration of H-NCs. Owing to the successful elimination of *S. aureus* biofilms and the modulated osteoimmune microenvironment, a substantially greater quantity of new bone tissue was observed at the interface between bone and H-NCs in the micro-computed tomography (micro-CT) images taken on both days 14 and 28 (Figure 6A). As shown in Figure 6B, the calculated bone volume/tissue volume (BV/TV) ratios for Ti-NIR(+) and

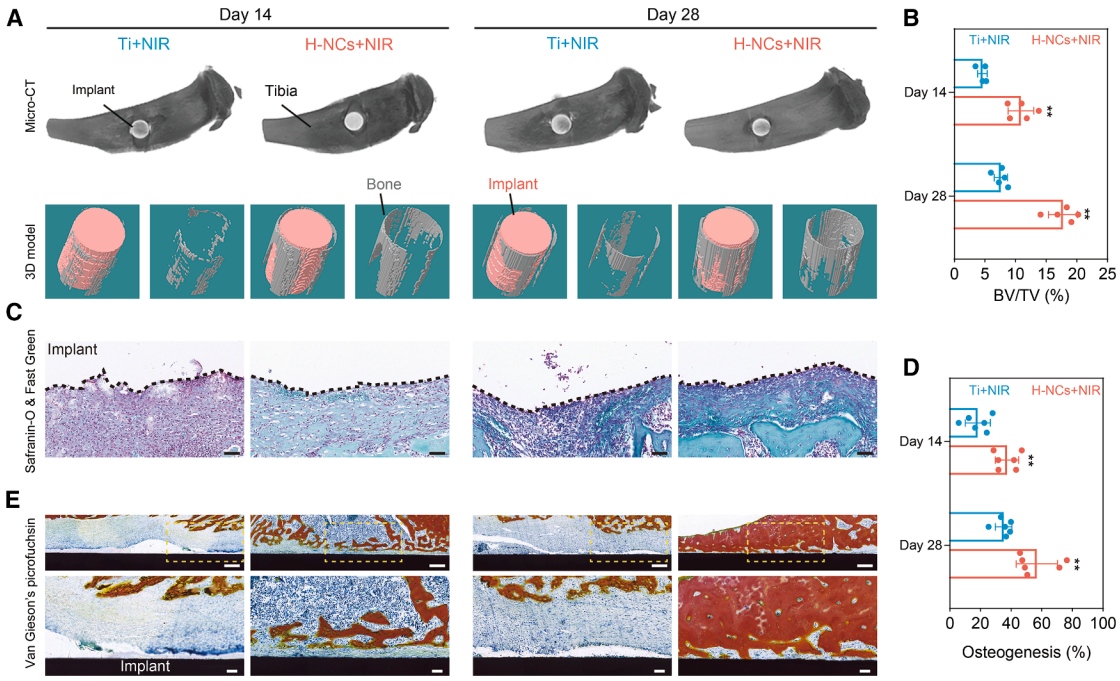

Figure 6. Evaluation of *in vivo* bone-to-implant integration

(A) 3D reconstructed micro-CT results.

(B) Quantification of newly formed bone volume around the implants (BV/TV) based on micro-CT results.

(C) Representative safranin-O and fast green staining images of tissue near the implants. Scale bars, 50 μm.

(D) Semi-quantitative analysis of safranin-O and fast green staining images.

(E) Van Gieson's picrofuchsin staining images. Scale bars, 200 μm (upper), 50 μm (lower). $n \geq 3$ independent experiments per group. $p < 0.05$, $p < 0.01$. Data are presented as mean ± SD.

H-NCs-NIR(+) at day 14 were 4.58% and 11.42%, respectively. On day 28, the BV/TV values for Ti-NIR(+) and H-NCs-NIR(+) were 7.3% and 18.63%, respectively.

The osteogenic condition of the tissue surrounding the implant was evaluated utilizing safranin-O/fast green staining, with green indicating osteogenic differentiation and red representing cartilage differentiation (Figure 6C). As shown in the semi-quantified results in Figure 6D, a higher proportion of osteogenic differentiation was observed at the interface of H-NCs-NIR(+) compared with Ti-NIR (+) (the implant position is marked by a dashed line) on both days 14 and 28. In addition, almost no bone-like tissue (red) was observed at the bone-implant interface of Ti-NIR(+) in Van Gieson's picrofuchsin staining images (Figures 6E and S8). In contrast, a substantial area of bony tissue was clearly observed on the surface of H-NCs-NIR(+). These *in vivo* results conclusively demonstrated that H-NCs-NIR(+) could effectively eliminate *S. aureus* biofilms and enhance osteogenesis simultaneously.

Conclusions

In summary, we have successfully developed a hydrogenated TiO_2 surface pattern that achieved highly effective bacterial elimination through NIR-induced ROS and hyperthermia and enhanced osteogenesis via surface topography-induced osteoimmunomodulation. The introduction of oxygen vacancies enhanced NIR light absorption and improved electron-hole separation efficiency, contributing to the effective antibacterial performance observed both *in vitro* and *in vivo* within a short exposure period to exogenous NIR stimuli. Without the aid of additional components, this *in situ* treatment approach assures the osteoimmunomodulation and antibacterial capabilities. While this innovative strategy has demonstrated its potential in effectively addressing the challenges associated with post-implantation infections and simultaneously promoting bone-to-implant integration, its effectiveness in deeper joints such as the hip is constrained by the limited penetration depth of NIR light. Potential strategies to overcome this limitation include increasing the power density of the NIR light. However, this must be carefully balanced with safety considerations, such as controlling photothermal effects with pulsed light stimulation. Despite these limitations, we believe that this approach can contribute to the future management of implant-associated infections, demonstrating considerable promise for clinical translation and ultimately improving clinical outcomes.

METHODS

Preparation of H-NCs

Ti substrates with diameters of 32 and 6 mm, and rods with a diameter of 2 mm and length of 6 mm were purchased from Shunhang Metal Materials. The 32-mm diameter samples were used for *in vitro* cell culture experiments, while the 6 mm diameter samples were assigned for *in vitro* antibacterial tests and

Please cite this article in press as: Zhu et al., NIR-responsive hydrogenated TiO_2 nanoscale honeycomb surface pattern for rapid *S. aureus* biofilm elimination and enhanced osteogenesis, Cell Biomaterials (2025), https://doi.org/10.1016/j.celbio.2025.100213

other general assessments. Rod-shaped samples were utilized in *in vivo* studies. Monodispersed polystyrene spheres with 90 nm diameter were purchased from Yuan Biotech.

To obtain H-NCs, NCs were first prepared on Ti substrates following our previously established method.[39] In brief, polystyrene spheres were ultrasonically dispersed in ethanol and subsequently deposited onto a silicon slide positioned at the edge of a Petri dish containing 5.4 wt % $Ti(SO_4)_2$ solution, until a polystyrene monolayer film covered the solution surface. The resulting polystyrene monolayer film and $Ti(SO_4)_2$ solution were then placed in a preheated 50°C oven for 3 h, allowing TiO_2 to form at the lower part of the polystyrene spheres through $Ti(SO_4)_2$ hydrolysis. Following this, the film with formed TiO_2 was gently transferred onto Ti substrates and rods and allowed to dry at room temperature overnight. NCs were obtained after calcination at 500°C for 2 h to remove the template polystyrene spheres. Finally, H-NCs were acquired through hydrogen plasma treatment using a plasma-enhanced chemical vapor deposition (PE-CVD) system with a flow rate of 20 sccm, power of 100 W, and temperature of 500°C for 1 h.

Surface characterizations

The surface morphology was observed using a field emission SEM (Zeiss Sigma 500) after sputter-coating with gold, and the detailed microstructure was examined using HR-TEM (JEOL JEM-F200). The crystalline phase was analyzed by XRD (D8A25, Bruker) with a 2θ range from 20° to 80° and a step size of 0.02°. Elemental composition and chemical states were analyzed by XPS (ESCALAB 250Xi, Thermo Scientific) with Al Kα radiation and an energy step size of 0.100 eV; the binding energy scale was calibrated to the C 1s peak at 284.8 eV. Surface roughness was analyzed using AFM (FlexMount, Nanosurf). EPR spectra were obtained using an EPR spectrometer (Bruker EMXnano). UV-vis-NIR DRS were recorded with a UV-vis-NIR spectrometer (UV-3600, Shimadzu). PL spectra were acquired using a fluorescence spectrophotometer (Perkin-Elmer LS55).

Photodynamic and photothermal performance

An 808-nm laser source (FLMM-0808-862-005W, Hi-Tech Optoelectronics) was utilized as the irradiation source throughout this study. The photodynamic performance of various samples, in terms of ROS generation, was assessed using a DCFH-DA ROS assay kit. In brief, samples were immersed in the DCFH-DA solution and exposed to NIR (0.5 W cm^{-2}) for 15 min. The fluorescence intensity of DCF was measured at 525 nm using a microplate reader (SpectraMax i3, Molecular Devices). Current density and EIS were recorded using an electrochemical workstation (CHI660E, Shanghai Chenhua) with a three-electrode system. ROS levels in different samples were measured using an ESR spectrometer after being subjected to NIR irradiation for 0, 5, 10, and 15 min. In these ESR tests, 2,2,6,6-tetramethylpiperidine (TEMP) was employed for detecting singlet oxygen ($^1O_2$), while 5,5-dimethyl-1-pyrroline-N-oxide (DMPO) was used for detecting superoxide radicals ($\cdot O^{2-}$) and hydroxyl radicals (·OH).

The photothermal performance of various samples was examined under NIR irradiation. Samples were placed in a 96-well plate containing 200 μL PBS solution and exposed to NIR irradiation. Temperature changes were monitored using a thermal imager (FLIR, E52).

In vitro antibacterial activity assay

S. aureus strain (ATCC 29213) was used to evaluate the *in vitro* antibacterial performance of different samples. samples were sterilized under UV light for 30 min before use. Then, 200 μL bacteria suspension (1×10^7 colony-forming unit [CFU]/mL) was added into a 96-well plate with samples placed inside. For the NIR-treated group, the samples immersed in the bacterial suspension were exposed to NIR irradiation at a power density of 0.5 W/cm^2 for 15 min. For the non-NIR-treated group, the samples with bacterial suspension were kept in the dark at room temperature for 15 min. After treatment, the bacterial suspensions from each well were diluted 40,000-fold, and 20 μL of the diluted suspension was spread onto Luria-Bertani (LB) agar plates. The number of colonies on agar plates was counted to calculate the antibacterial efficiency of different samples using the following formula: antibacterial ratio (%) = [*N*(control) − *N*(experiment group)]/*N*(control) × 100%.

Live/dead bacteria staining

Bacteria treated on different samples were stained with two fluorescent dyes, DMAO and EthD-III, using a commercial live and dead bacterial staining kit (Yeasen Biotechnology) following the manufacturer's instructions. In brief, bacteria were cultured and treated with samples as described in the antibacterial test. Following this, the culture solution was replaced with DMAO/EthD-III working solution and incubated for 15 min in the dark. Fluorescence images of stained bacteria on different samples were obtained using an inverted fluorescence microscope (AMAFD2000, Evos FL Auto 2).

Bacterial morphology

After treatment on different samples with or without NIR irradiation, bacteria were fixed with 2.5% glutaraldehyde and dehydrated with a gradient ethanol solution (30%–100%). The bacterial morphologies of *S. aureus* on different sample surfaces were observed using an SEM (Zeiss Sigma 500).

Protein leakage

A BCA protein assay kit (Solarbio) was used to measure protein leakage from *S. aureus*. The bacterial suspension was first centrifuged and washed with PBS (4°C, 6,000 rpm, 5 min) three times. The collected bacteria were then re-dispersed in PBS and diluted to an OD of 0.05–0.1 at 600 nm. Then, the diluted bacterial dispersion was treated with samples as described in the antibacterial test. After treatment, the bacteria were collected by centrifugation (4°C, 6,000 rpm, 5 min). The resulting supernatants (25 μL) were then mixed with the BCA working solution following the manufacturer's instructions and incubated at 37°C for 30 min. The OD value at 562 nm was measured using a microplate reader.

Bacterial membrane permeability

ONPG was utilized to evaluate the changes in membrane permeability of *S. aureus* treated with various samples, modified from

Please cite this article in press as: Zhu et al., NIR-responsive hydrogenated TiO_2 nanoscale honeycomb surface pattern for rapid *S. aureus* biofilm elimination and enhanced osteogenesis, Cell Biomaterials (2025), https://doi.org/10.1016/j.celbio.2025.100213

our previously reported method.[76] Briefly, *S. aureus* was first cultured in LB medium with 10 μg mL^{-1} of isopropyl β-D-1-thiogalactopyranoside (IPTG, Sinopharm Chemical Reagent) at 37°C for 12 h. The bacteria were then centrifuged and washed with PBS three times at a speed of 6,000 rpm. The resulting bacteria were diluted and treated with different samples, with or without NIR irradiation as described earlier. Finally, 15 μL treated bacteria was mixed with 15 μL ONPG (Sinopharm Chemical Reagent), 10 μL dimethyl sulfoxide (7%), and 110 μL PBS in 96-well plates. The OD value was measured at 420 nm.

Macrophage culture

RAW 264.7 macrophages were cultured in Dulbecco's modified Eagle's medium (HyClone) containing 1% penicillin-streptomycin (Gibco) and 10% fetal bovine serum (Gibco). Cells were incubated at 37°C in a 5% CO_2 atmosphere, with the culture medium replaced daily. The modulatory effects of different samples on macrophages, including alterations in cell morphology, macrophage polarization, and cytokine secretion levels were investigated.

Cell morphology observation under SEM

Cell suspension of RAW 264.7 macrophages (1×10^5 cells/mL) was cultured on different samples for 24 h, then fixed with 2.5% glutaraldehyde for 2 h, and sequentially dehydrated with ethanol (30%–100%). The cell morphologies of RAW 264.7 macrophages on different samples were examined using an SEM (Hitachi S4800 FEG SEM).

Immunofluorescence staining

The RAW 264.7 macrophages were cultured on samples for 48 h, then fixed with 4% paraformaldehyde for 20 min, permeabilized with 0.25% Triton X for 20 min, and blocked by 1% bovine serum albumin for 1 h. Cells on the samples were then incubated with primary antibodies against CD206 and iNOS (Abcam) at a 1:100 dilution at 4°C overnight. Next, cells were incubated with Alexa Fluor 488 conjugate anti-mouse secondary antibody for 30 min and stained with DAPI. Immunofluorescence-stained cells on the samples were observed using a confocal laser scanning microscope (Zeiss, LSM 800).

Quantitative real-time PCR

Total RNA from cells cultured on different samples for 24 and 48 h was first isolated using an RNA kit (OMEGA) following the manufacturer's instructions. The isolated RNA was reverse-transcribed to cDNA using PrimeScript RT Master Mix (TaKaRa). Real-time qPCR was performed on a QuantStudio 5 Real-Time PCR System (Thermo Fisher Scientific) for internal reference for GAPDH, M1 markers TNF-α and IL-1β, and M2 markers IL-10 and ARG-1. The synthesized primers are shown in Table S3.

ELISA

To measure the cytokines produced by macrophages cultured on different samples, macrophages were first cultured on samples for 24 and 48 h to collect supernatants. The secretion of cytokines TNF-α, IL-1β, IL-10, ARG-1, and BMP-2 was then measured using commercial ELISA kits (Shanghai Jianglai Industry).

Transcriptomic analysis

RAW 264.7 macrophages were cultured on samples for 48 h as mentioned above. After culturing, macrophages on samples were lysed by trizol reagent (Thermo Fisher Scientific) and stored at −80°C before sequencing. RNA sequencing was performed using Illumina HiSeq X10 (Illumina). The value of gene expression was transformed as $\log_{10}$ (transcripts per million reads [TPM] + 1). The data analysis and visualization were performed using a free online platform (www.bioinformatics.com.cn).

In vivo evaluation

All animal experiments were approved by the Animal Research Committee of Bestcell Model Biological Center, Wuhan, China (ethics approval number, BSMS 2024-06-07A). Male Sprague-Dawley rats (250–300 g) were randomly divided into three batches for three time points (days 2, 14, and 28) and two groups: Ti + NIR(+) and H-NCs + NIR(+) ($n \geq 3$ at each time point). Before implantation, rod-shaped samples were cultured in *S. aureus* suspension (1×10^7 CFU/mL) at 37°C for 48 h. Animals were anesthetized with pentobarbital (30 mg/kg, 1% [w/w]). Defects were then created in the tibia plateau area of the rats using a 2-mm-diameter twist drill bit at 8,000 rpm. During drilling, physiological saline was used for cooling until the bone marrow was exposed. Following the drilling procedure, the surgical area was cleaned using gauze. The samples were then slightly pressed to fit into the defects on both legs of the rats, and the wounds were finally sutured. 2 days after surgery, 15 min of NIR irradiation were applied to the surgical area. One batch of animals were sacrificed after NIR treatment, and the corresponding samples were removed for *in vivo* antibacterial activity assay. The collected samples were rolled on agar plates and incubated at 37°C for 24 h. The number of colonies was counted to calculate the antibacterial efficiency. The other two batches of animals were sacrificed 14 and 28 days after surgery for micro-CT and histopathological analysis.

Micro-CT analysis

Micro-CT analysis was conducted using a micro-CT system (SkyScan 1176, SkyScan) to examine the harvested tibias with implants. The major scanning parameters included an 80 kV source voltage, 313 μA source current, and 345 ms exposure time. The acquired scan images were reconstructed with the CTvox and CTVol software (SkyScan) to generate 3D representations of the overall bone morphology and microarchitecture around the implants. The region of interest (ROI) was defined as a 180-μm circular band extending radially outward from the implant surface, in line with referenced methodologies.[77] New bone volume (BV/TV) values were determined using the Data Viewer and CTan Program (Skyscan).

Histopathological analysis

The harvested samples were randomly allocated for further histopathological analysis. Following decalcification, the samples were embedded in paraffin, sectioned at 5-μm thickness, and

stained with Giemsa, as well as safranin-O and fast green. Immunohistochemistry staining was performed using antibodies for CD68 (Boster), TNF-α (Bioss), and IL-10 (Bioss).

Tissue morphologies were digitally scanned using a digital slide scanner (3DHistech Pannoramic Midi) and analyzed with CaseViewer software (3DHistech). For both immunohistochemistry staining images and safranin-O and fast green staining images, random samples from each group ($n = 6$) were selected for semi-quantitative analysis using the Image-Pro Plus software. Specifically, the analysis of safranin-O and fast green staining images assessed the osteogenesis ratio (green representing osteogenesis, while red or orange indicated cartilage) within a region extending approximately 200 μm from the implant surface.

For Van Gieson's picrofuchsin staining, hard tissue processing was conducted according to our previous study.[78] The embedded samples were sectioned longitudinally along the implant and ground to a thickness of 50–70 μm before being stained with Van Gieson's picrofuchsin. Images of the Van Gieson's picrofuchsin staining were obtained using a digital slide scanner.

Statistical analysis

All experiments were evaluated as mean values ± standard deviation of at least three tests. A one-way analysis of variance (ANOVA) program combined with a Student's t test was used to evaluate the statistical significance of the variance. Values of $^{*}p < 0.05$ and $^{**}p < 0.01$ were considered statistically significant.

RESOURCE AVAILABILITY

Lead contact

Further information and requests for resources and reagents should be directed to and will be fulfilled by the lead contact, Kelvin W.K. Yeung (wkkyeung@hku.hk).

Materials availability

This study did not generate new, unique reagents.

Data and code availability

The data supporting this study's findings are available from the lead contact upon reasonable request.

ACKNOWLEDGMENTS

This work is jointly supported by the National Key R&D Program of China (no. 2023YFB3810200), the General Research Fund of the Research Grants Council (nos. 17214516, 17207719, and 1711322), the Hong Kong Innovation Technology Fund (no. ITS/256/22), the Health and Medical Research Fund (nos. 20190244, 21200592, 22210832, 23220952, and 09201466), the Collaborative Research Fund of the Research Grants Council (nos. C5044-21G and C7003-22Y), the National Natural Science Foundation of China (nos. 82201124 and 52173251), Shenzhen Science and Technology Funding (nos. SGDX20220530111405038, JCYJ20210324120009026, and JCYJ20210324120012034), the Guangdong Basic and Applied Basic Research Foundation (no. 2023A1515011963), the National Natural Science Foundation of China/Research Grants Council Joint Research Scheme (no. N_HKU721/23), the National Science Fund for Distinguished Youth Scholar (no. 51925104), the Central Guidance on Local Science and Technology Development Fund of Hebei Province (no. 226Z1303G), the Yanzhao Young Scientist Project (no. C2023202018), and the Beijing Natural Science Foundation (no. 7232338).

AUTHOR CONTRIBUTIONS

Y.Z. and K.W.K.Y. conceived and designed the experimental concept. Y.Z. and J.Q. synthesized the materials and performed material characterizations. Y.Z. and C.A. carried out the *in vitro* and *in vivo* experiments. Y.Z. analyzed the experimental data, and together with C.A. co-wrote the manuscript. Y.X., C. M., J.W., W.Q., Xiangmei Liu, S.W., Xuanyong Liu, X.Z., B.L., and K.W.K.Y. contributed valuable experimental insights. Xiangmei Liu, S.W., Xuanyong Liu, and K.W.K.Y. provided funding support and resources for the study. All the authors discussed, commented, and agreed on the manuscript.

DECLARATION OF INTERESTS

The authors declare no competing interests.

SUPPLEMENTAL INFORMATION

Supplemental information can be found online at https://doi.org/10.1016/j.celbio.2025.100213.

Received: February 5, 2025
Revised: May 8, 2025
Accepted: August 22, 2025

REFERENCES

1. Siddiqi, A., Levine, B.R., and Springer, B.D. (2022). Highlights of the 2021 American joint replacement registry annual report. Arthroplast. Today *13*, 205–207. https://doi.org/10.1016/j.artd.2022.01.020.
2. Hegde, V., Stambough, J.B., Levine, B.R., and Springer, B.D. (2023). Highlights of the 2022 American joint replacement registry annual report. Arthroplast. Today *21*, 101137. https://doi.org/10.1016/j.artd.2023.101137.
3. Ryan, S.P., Stambough, J.B., Huddleston, J.I., III, and Levine, B.R. (2024). Highlights of the 2023 American Joint Replacement Registry Annual Report. Arthroplast. Today *26*, 101325. https://doi.org/10.1016/j.artd.2024.101325.
4. Trampuz, A., and Widmer, A.F. (2006). Infections associated with orthopedic implants. Curr. Opin. Infect. Dis. *19*, 349–356. https://doi.org/10.1097/01.qco.0000235161.85925.e8.
5. Moriarty, T.F., Kuehl, R., Coenye, T., Metsemakers, W.-J., Morgenstern, M., Schwarz, E.M., Riool, M., Zaat, S.A.J., Khana, N., Kates, S.L., et al. (2016). Orthopaedic device-related infection: current and future interventions for improved prevention and treatment. EFORT Open Rev. *1*, 89–99. https://doi.org/10.1302/2058-5241.1.000037.
6. Ghosh, S., Sinha, M., Samanta, R., Sadhasivam, S., Bhattacharyya, A., Nandy, A., Saini, S., Tandon, N., Singh, H., Gupta, S., et al. (2022). A potent antibiotic-loaded bone-cement implant against staphylococcal bone infections. Nat. Biomed. Eng. *6*, 1180–1195. https://doi.org/10.1038/s41551-022-00950-x.
7. Bernard, L., Arvieux, C., Brunschweiler, B., Touchais, S., Ansart, S., Bru, J.-P., Oziol, E., Boeri, C., Gras, G., Druon, J., et al. (2021). Antibiotic therapy for 6 or 12 weeks for prosthetic joint infection. N. Engl. J. Med. *384*, 1991–2001. https://doi.org/10.1056/NEJMoa2020198.
8. Ahmadi, H., Ebrahimi, A., and Ahmadi, F. (2021). Antibiotic therapy in dentistry. Int. J. Dent. *2021*, 6667624. https://doi.org/10.1155/2021/6667624.
9. Isefuku, S., Joyner, C.J., and Simpson, A.H.R. (2003). Gentamicin may have an adverse effect on osteogenesis. J. Orthop. Trauma *17*, 212–216. https://doi.org/10.1097/00005131-200303000-00010.
10. Steckelberg, J.M., and Osmon, D.R. (2000). Prosthetic Joint Infections. In Infections Associated with Indwelling Medical Devices, Third Edition (ASM Press), pp. 173–209.

11. Otten, M.R., Kildow, B.J., Sayles, H.R., Drummond, D., and Garvin, K.L. (2021). Two-stage reimplantation of a prosthetic hip infection: systematic review of long-term reinfection and pathogen outcomes. J. Arthroplasty *36*, 2630–2641. https://doi.org/10.1016/j.arth.2021.02.046.

12. Wilde, A.H., and Ruth, J.T. (1988). Two-stage reimplantation in infected total knee arthroplasty. Clin. Orthop. Relat. Res., 23–35. https://doi.org/10.1097/00003086-198811000-00004.

13. Wignadasan, W., Ibrahim, M., and Haddad, F.S. (2023). One-or two-stage reimplantation for infected total knee prosthesis? Orthop. Traumatol. Surg. Res. *109*, 103453. https://doi.org/10.1016/j.otsr.2022.103453.

14. Cortes-Penfield, N., Krsak, M., Damioli, L., Henry, M., Seidelman, J., Hewlett, A., and Certain, L. (2024). How We Approach Suppressive Antibiotic Therapy Following Debridement, Antibiotics, and Implant Retention for Prosthetic Joint Infection. Clin. Infect. Dis. *78*, 188–198. https://doi.org/10.1093/cid/ciad484.

15. Fisher, R.A., Gollan, B., and Helaine, S. (2017). Persistent bacterial infections and persister cells. Nat. Rev. Microbiol. *15*, 453–464. https://doi.org/10.1038/nrmicro.2017.42.

16. Arciola, C.R., Campoccia, D., and Montanaro, L. (2018). Implant infections: adhesion, biofilm formation and immune evasion. Nat. Rev. Microbiol. *16*, 397–409. https://doi.org/10.1038/s41579-018-0019-y.

17. Stigter, M., Bezemer, J., De Groot, K., and Layrolle, P. (2004). Incorporation of different antibiotics into carbonated hydroxyapatite coatings on titanium implants, release and antibiotic efficacy. J. Control. Release *99*, 127–137. https://doi.org/10.1016/j.jconrel.2004.06.011.

18. Xie, K., Zhou, Z., Guo, Y., Wang, L., Li, G., Zhao, S., Liu, X., Li, J., Jiang, W., Wu, S., et al. (2019). Long-term prevention of bacterial infection and enhanced osteoinductivity of a hybrid coating with selective silver toxicity. Adv. Healthc. Mater. *8*, e1801465. https://doi.org/10.1002/adhm.201801465.

19. Zhu, Y., Liu, X., Yeung, K.W.K., Chu, P.K., and Wu, S. (2017). Biofunctionalization of carbon nanotubes/chitosan hybrids on Ti implants by atom layer deposited ZnO nanostructures. Appl. Surf. Sci. *400*, 14–23. https://doi.org/10.1016/j.apsusc.2016.12.158.

20. Rivera, L.R., Cochis, A., Biser, S., Canciani, E., Ferraris, S., Rimondini, L., and Boccaccini, A.R. (2021). Antibacterial, pro-angiogenic and pro-osteointegrative zein-bioactive glass/copper based coatings for implantable stainless steel aimed at bone healing. Bioact. Mater. *6*, 1479–1490. https://doi.org/10.1016/j.bioactmat.2020.11.001.

21. Sun, Z., Ma, L., Sun, X., Sloan, A.J., O'Brien-Simpson, N.M., and Li, W. (2023). The overview of antimicrobial peptide-coated implants against oral bacterial infections. Aggregate *4*, e309. https://doi.org/10.1002/agt2.309.

22. Sandhu, A.K., Yang, Y., and Li, W.-W. (2022). In vivo antibacterial efficacy of antimicrobial peptides modified metallic Implants-Systematic review and meta-analysis. ACS Biomater. Sci. Eng. *8*, 1749–1762. https://doi.org/10.1021/acsbiomaterials.1c01307.

23. Makvandi, P., Wang, C.y., Zare, E.N., Borzacchiello, A., Niu, L.n., and Tay, F.R. (2020). Metal-based nanomaterials in biomedical applications: antimicrobial activity and cytotoxicity aspects. Adv. Funct. Mater. *30*, 1910021. https://doi.org/10.1002/adfm.201910021.

24. Campoccia, D., Montanaro, L., and Arciola, C.R. (2013). A review of the biomaterials technologies for infection-resistant surfaces. Biomaterials *34*, 8533–8554. https://doi.org/10.1016/j.biomaterials.2013.07.089.

25. Tan, L., Fu, J., Feng, F., Liu, X., Cui, Z., Li, B., Han, Y., Zheng, Y., Yeung, K.W.K., Li, Z., et al. (2020). Engineered probiotics biofilm enhances osseointegration via immunoregulation and anti-infection. Sci. Adv. *6*, eaba5723. https://doi.org/10.1126/sciadv.aba5723.

26. Jiang, P., Zhang, Y., Hu, R., Shi, B., Zhang, L., Huang, Q., Yang, Y., Tang, P., and Lin, C. (2023). Advanced surface engineering of titanium materials for biomedical applications: From static modification to dynamic responsive regulation. Bioact. Mater. *27*, 15–57. https://doi.org/10.1016/j.bioactmat.2023.03.006.

27. Zheng, Q., Liu, X., Zheng, Y., Yeung, K.W.K., Cui, Z., Liang, Y., Li, Z., Zhu, S., Wang, X., and Wu, S. (2021). The recent progress on metal-organic frameworks for phototherapy. Chem. Soc. Rev. *50*, 5086–5125. https://doi.org/10.1039/d1cs00056j.

28. Tan, L., Li, J., Liu, X., Cui, Z., Yang, X., Zhu, S., Li, Z., Yuan, X., Zheng, Y., Yeung, K.W.K., et al. (2018). Rapid biofilm eradication on bone implants using red phosphorus and near-infrared light. Adv. Mater. *30*, e1801808. https://doi.org/10.1002/adma.201801808.

29. Li, Y., Xu, X., Liu, X., Li, B., Han, Y., Zheng, Y., Chen, D.F., Yeung, K.W.K., Cui, Z., Li, Z., et al. (2020). Photoelectrons mediating angiogenesis and immunotherapy through heterojunction film for noninvasive disinfection. Adv. Sci. (Weinh) *7*, 2000023. https://doi.org/10.1002/advs.202000023.

30. Li, M., Li, L., Su, K., Liu, X., Zhang, T., Liang, Y., Jing, D., Yang, X., Zheng, D., Cui, Z., et al. (2019). Highly effective and noninvasive near-infrared eradication of a Staphylococcus aureus biofilm on implants by a photoresponsive coating within 20 min. Adv. Sci. (Weinh) *6*, 1900599. https://doi.org/10.1002/advs.201900599.

31. Mao, C., Zhu, W., Xiang, Y., Zhu, Y., Shen, J., Liu, X., Wu, S., Cheung, K.M.C., and Yeung, K.W.K. (2021). Enhanced near-infrared photocatalytic eradication of MRSA biofilms and osseointegration using oxide perovskite-based P–N heterojunction. Adv. Sci. (Weinh) *8*, e2002211. https://doi.org/10.1002/advs.202002211.

32. Addison, O., Davenport, A.J., Newport, R.J., Kalra, S., Monir, M., Mosselmans, J.F., Proops, D., and Martin, R.A. (2012). Do 'passive' medical titanium surfaces deteriorate in service in the absence of wear? J. R. Soc. Interface *9*, 3161–3164. https://doi.org/10.1098/rsif.2012.0438.

33. Chen, X., Shen, S., Guo, L., and Mao, S.S. (2010). Semiconductor-based Photocatalytic Hydrogen Generation. Chem. Rev. *110*, 6503–6570. https://doi.org/10.1021/cr1001645.

34. Wu, S., and Butt, H.J. (2016). Near-infrared-sensitive materials based on upconverting nanoparticles. Adv. Mater. *28*, 1208–1226. https://doi.org/10.1002/adma.201502843.

35. Lepcha, A., Maccato, C., Mettenbörger, A., Andreu, T., Mayrhofer, L., Walter, M., Olthof, S., Ruoko, T.P., Klein, A., Moseler, M., et al. (2015). Electrospun black titania nanofibers: influence of hydrogen plasma-induced disorder on the electronic structure and photoelectrochemical performance. J. Phys. Chem. C *119*, 18835–18842. https://doi.org/10.1021/acs.jpcc.5b02767.

36. Hu, Y.H. (2012). A Highly Efficient Photocatalyst—Hydrogenated Black TiO2 for the Photocatalytic Splitting of Water. Angew. Chem. Int. Ed. *51*, 12410–12412. https://doi.org/10.1002/anie.201206375.

37. Yan, Y., Han, M., Konkin, A., Koppe, T., Wang, D., Andreu, T., Chen, G., Vetter, U., Morante, J.R., and Schaaf, P. (2014). Slightly hydrogenated TiO_2 with enhanced photocatalytic performance. J. Mater. Chem. A *2*, 12708–12716. https://doi.org/10.1039/C4TA02192D.

38. Zhu, Y., Liu, X., Wu, J., Wong, T.M., Feng, X., Yang, C., Wu, S., Zheng, Y., Liu, X., and Cheung, K.M. (2019). Micro-and nanohemispherical 3D imprints modulate the osteogenic differentiation and mineralization tendency of bone cells. ACS Appl. Mater. Interfaces *11*, 35513–35524.

39. Zhu, Y., Liang, H., Liu, X., Wu, J., Yang, C., Wong, T.M., Kwan, K.Y.H., Cheung, K.M.C., Wu, S., and Yeung, K.W.K. (2021). Regulation of macrophage polarization through surface topography design to facilitate implant-to-bone osteointegration. Sci. Adv. *7*, eabf6654. https://doi.org/10.1126/sciadv.abf6654.

40. Moongraksathum, B., Hsu, P.-T., and Chen, Y.-W. (2016). Photocatalytic activity of ascorbic acid-modified TiO_2 sol prepared by the peroxo sol–gel method. J. Sol Gel Sci. Technol. *78*, 647–659. https://doi.org/10.1007/s10971-016-3993-4.

41. Su, K., Tan, L., Liu, X., Cui, Z., Zheng, Y., Li, B., Han, Y., Li, Z., Zhu, S., Liang, Y., et al. (2020). Rapid photo-sonotherapy for clinical treatment of bacterial infected bone implants by creating oxygen deficiency using sulfur doping. ACS Nano *14*, 2077–2089. https://doi.org/10.1021/acsnano.9b08686.

42. Wu, T., Zhao, H., Zhu, X., Xing, Z., Liu, Q., Liu, T., Gao, S., Lu, S., Chen, G., Asiri, A.M., et al. (2020). Identifying the origin of Ti3+ activity toward enhanced electrocatalytic N_2 reduction over TiO_2 nanoparticles modulated by mixed-valent copper. Adv. Mater. *32*, e2000299. https://doi.org/10.1002/adma.202000299.

43. Sun, Z.X., Sun, K., Gao, M.L., Metin, Ö., and Jiang, H.L. (2022). Optimizing Pt electronic states through formation of a schottky junction on non-reducible metal–organic frameworks for enhanced photocatalysis. Angew. Chem. Int. Ed. Engl. *61*, e202206108. https://doi.org/10.1002/anie.202206108.

44. Pallotti, D.K., Passoni, L., Gesuele, F., Maddalena, P., Di Fonzo, F., and Lettieri, S. (2017). Giant O_2-induced photoluminescence modulation in hierarchical titanium dioxide nanostructures. ACS Sens. *2*, 61–68. https://doi.org/10.1021/acssensors.6b00432.

45. Abdi, F.F., Han, L., Smets, A.H.M., Zeman, M., Dam, B., and Van De Krol, R. (2013). Efficient solar water splitting by enhanced charge separation in a bismuth vanadate-silicon tandem photoelectrode. Nat. Commun. *4*, 2195. https://doi.org/10.1038/ncomms3195.

46. Zhang, Q., Liu, X., Tan, L., Cui, Z., Li, Z., Liang, Y., Zhu, S., Yeung, K.W.K., Zheng, Y., and Wu, S. (2020). An UV to NIR-driven platform based on red phosphorus/graphene oxide film for rapid microbial inactivation. Chem. Eng. J. *383*, 123088. https://doi.org/10.1016/j.cej.2019.123088.

47. Zhang, W., Li, Y., and Peng, S. (2016). Facile synthesis of graphene sponge from graphene oxide for efficient dye-sensitized H2 evolution. ACS Appl. Mater. Interfaces *8*, 15187–15195. https://doi.org/10.1021/acsami.6b01805.

48. Wang, Z., Yang, C., Lin, T., Yin, H., Chen, P., Wan, D., Xu, F., Huang, F., Lin, J., Xie, X., et al. (2013). Visible-light photocatalytic, solar thermal and photoelectrochemical properties of aluminium-reduced black titania. Energy Environ. Sci. *6*, 3007–3014. https://doi.org/10.1039/c3ee41817k.

49. Hua, Z., Li, B., Li, L., Yin, X., Chen, K., and Wang, W. (2017). Designing a novel photothermal material of hierarchical microstructured copper phosphate for solar evaporation enhancement. J. Phys. Chem. C *121*, 60–69. https://doi.org/10.1021/acs.jpcc.6b08975.

50. Wang, G., Wang, H., Ling, Y., Tang, Y., Yang, X., Fitzmorris, R.C., Wang, C., Zhang, J.Z., and Li, Y. (2011). Hydrogen-treated TiO2 nanowire arrays for photoelectrochemical water splitting. Nano Lett. *11*, 3026–3033. https://doi.org/10.1021/nl201766h.

51. Li, X., Kang, B., Dong, F., Zhang, Z., Luo, X., Han, L., Huang, J., Feng, Z., Chen, Z., Xu, J., et al. (2021). Enhanced photocatalytic degradation and H_2/H_2O_2 production performance of S-pCN/WO_2. Nano Energy *81*, 105671. https://doi.org/10.1016/j.nanoen.2020.105671.

52. Chen, X., Liu, L., Yu, P.Y., and Mao, S.S. (2011). Increasing solar absorption for photocatalysis with black hydrogenated titanium dioxide nanocrystals. Science *331*, 746–750. https://doi.org/10.1126/science.1200448.

53. Yang, Y., Ma, L., Cheng, C., Deng, Y., Huang, J., Fan, X., Nie, C., Zhao, W., and Zhao, C. (2018). Nonchemotherapic and robust dual-responsive nanoagents with on-demand bacterial trapping, ablation, and release for efficient wound disinfection. Adv. Funct. Mater. *28*, 1705708. https://doi.org/10.1002/adfm.201705708.

54. Tan, L., Zhou, Z., Liu, X., Li, J., Zheng, Y., Cui, Z., Yang, X., Liang, Y., Li, Z., Feng, X., et al. (2020). Overcoming multidrug-resistant MRSA using conventional aminoglycoside antibiotics. Adv. Sci. (Weinh) *7*, 1902070. https://doi.org/10.1002/advs.201902070.

55. Li, J., Tan, L., Liu, X., Cui, Z., Yang, X., Yeung, K.W.K., Chu, P.K., and Wu, S. (2017). Balancing bacteria–osteoblast competition through selective physical puncture and biofunctionalization of ZnO/polydopamine/arginine-glycine-aspartic acid-cysteine nanorods. ACS Nano *11*, 11250–11263. https://doi.org/10.1021/acsnano.7b05620.

56. Li, Y., Liu, X., Tan, L., Cui, Z., Jing, D., Yang, X., Liang, Y., Li, Z., Zhu, S., Zheng, Y., et al. (2019). Eradicating multidrug-resistant bacteria rapidly using a multi functional g-C_3N_4@Bi_2S_3 nanorod heterojunction with or without antibiotics. Adv. Funct. Mater. *29*, 1900946. https://doi.org/10.1002/adfm.201900946.

57. Mountziaris, P.M., and Mikos, A.G. (2008). Modulation of the inflammatory response for enhanced bone tissue regeneration. Tissue Eng. Part B Rev. *14*, 179–186. https://doi.org/10.1089/ten.teb.2008.0038.

58. Chen, Z., Klein, T., Murray, R.Z., Crawford, R., Chang, J., Wu, C., and Xiao, Y. (2016). Osteoimmunomodulation for the development of advanced bone biomaterials. Mater. Today *19*, 304–321. https://doi.org/10.1016/j.mattod.2015.11.004.

59. Han, X., Shen, J., Chen, S., Cai, Z., Zhu, Y., Yi, W., Li, K., Cai, W., Tao, B., Cui, W., et al. (2023). Ultrasonic-controlled "explosive" hydrogels to precisely regulate spatiotemporal osteoimmune disturbance. Biomaterials *295*, 122057. https://doi.org/10.1016/j.biomaterials.2023.122057.

60. Nathan, K., Lu, L.Y., Lin, T., Pajarinen, J., Jämsen, E., Huang, J.-F., Romero-Lopez, M., Maruyama, M., Kohno, Y., Yao, Z., et al. (2019). Precise immunomodulation of the M1 to M2 macrophage transition enhances mesenchymal stem cell osteogenesis and differs by sex. Bone Joint Res. *8*, 481–488. https://doi.org/10.1302/2046-3758.810.BJR-2018-0231.R2.

61. Qiao, W., Wong, K.H.M., Shen, J., Wang, W., Wu, J., Li, J., Lin, Z., Chen, Z., Matinlinna, J.P., Zheng, Y., et al. (2021). TRPM7 kinase-mediated immunomodulation in macrophage plays a central role in magnesium ion-induced bone regeneration. Nat. Commun. *12*, 2885. https://doi.org/10.1038/s41467-021-23005-2.

62. Qiao, W., Pan, D., Zheng, Y., Wu, S., Liu, X., Chen, Z., Wan, M., Feng, S., Cheung, K.M.C., Yeung, K.W.K., et al. (2022). Divalent metal cations stimulate skeleton interoception for new bone formation in mouse injury models. Nat. Commun. *13*, 535. https://doi.org/10.1038/s41467-022-28203-0.

63. Sen, A., Qamar, R., Choubisa, R., Parikh, M., and Shah, D. (2025). BMP Modulation of Osteogenesis: Molecular Interactions and Clinical Applications (Springer), pp. 1–7. https://doi.org/10.1007/s43538-025-00400-7.

64. Zhu, Y., Wang, C., Ai, C., Xiang, Y., Mao, C., Qiao, W., Wu, J., Kubi, J.A., Liu, X., and Wu, S. (2024). Photocurrent-directed immunoregulation accelerates osseointegration through activating calcium influx in macrophages. Adv. Funct. *34*, 2406095.

65. Mahon, O.R., Browe, D.C., Gonzalez-Fernandez, T., Pitacco, P., Whelan, I.T., Von Euw, S., Hobbs, C., Nicolosi, V., Cunningham, K.T., Mills, K.H.G., et al. (2020). Nano-particle mediated M2 macrophage polarization enhances bone formation and MSC osteogenesis in an IL-10 dependent manner. Biomaterials *239*, 119833. https://doi.org/10.1016/j.biomaterials.2020.119833.

66. Liu, Q., Zhang, S., Shi, L., Shi, J., Sun, C., Wang, J., Zhou, W., Zhou, H., Shan, F., Wang, H., et al. (2024). Osteogenic induction and anti-inflammatory effects of calcium-chlorogenic acid nanoparticles remodel the osteoimmunology microenvironment for accelerating bone repair. Adv. Healthc. Mater. *13*, e2401114. https://doi.org/10.1002/adhm.202401114.

67. Davies, J.E. (1985). Exoemission for Biomaterials Research. Jpn. J. Appl. Phys. *24*, 43. https://doi.org/10.7567/JJAPS.24S4.43.

68. Niu, J., Guo, Y., Jing, G., Wang, H., Yang, L., Li, Y., Gao, Y., Wang, H., Li, A., Xu, X., et al. (2024). Anion-dependent layered double hydroxide nanoparticles regulate differentiation of cd206+ cx3cr1+ macrophages by inhibiting the IL-17 signaling pathway contributing to inflammatory bowel disease. Adv. Funct. Mater. *34*, 2305042. https://doi.org/10.1002/adfm.202305042.

69. Liu, L., Guo, H., Song, A., Huang, J., Zhang, Y., Jin, S., Li, S., Zhang, L., Yang, C., and Yang, P. (2020). Progranulin inhibits LPS-induced macrophage M1 polarization via NF-κB and MAPK pathways. BMC Immunol. *21*, 32. https://doi.org/10.1186/s12865-020-00355-y.

70. Ma, G., Pan, P.-Y., Eisenstein, S., Divino, C.M., Lowell, C.A., Takai, T., and Chen, S.-H. (2011). Paired immunoglobin-like receptor-B regulates the suppressive function and fate of myeloid-derived suppressor cells. Immunity *34*, 385–395. https://doi.org/10.1016/j.immuni.2011.02.004.

71. Franchi, L., Park, J.H., Shaw, M.H., Marina-Garcia, N., Chen, G., Kim, Y.G., and Núñez, G. (2008). Intracellular NOD-like receptors in innate

immunity, infection and disease. Cell. Microbiol. *10*, 1–8. https://doi.org/10.1111/j.1462-5822.2007.01059.x.

72. Zhou, F., Mei, J., Han, X., Li, H., Yang, S., Wang, M., Chu, L., Qiao, H., and Tang, T. (2019). Kinsenoside attenuates osteoarthritis by repolarizing macrophages through inactivating NF-κB/MAPK signaling and protecting chondrocytes. Acta Pharm. Sin. B *9*, 973–985. https://doi.org/10.1016/j.apsb.2019.01.015.
73. Yu, T., Gao, M., Yang, P., Liu, D., Wang, D., Song, F., Zhang, X., and Liu, Y. (2019). Insulin promotes macrophage phenotype transition through PI3K/Akt and PPAR-γ signaling during diabetic wound healing. J. Cell. Physiol. *234*, 4217–4231. https://doi.org/10.1002/jcp.27185.
74. Heron-Milhavet, L., and Djiane, A. (2022). MAGIs: Junctional scaffolds linking inter-cellular junction architecture, actin cytoskeleton dynamics, and signaling pathways. J. Cell Signal. *3*, 141–147.
75. Liu, Y., Luo, Z., Xie, Y., Sun, Y., Yuan, F., Jiang, L., Lu, H., and Hu, J. (2024). Extracellular vesicles from UTX-knockout endothelial cells boost neural stem cell differentiation in spinal cord injury. Cell Commun. Signal. *22*, 155. https://doi.org/10.1186/s12964-023-01434-4.
76. Zhu, Y., Hong, W., Liu, X., Tan, L., Wu, J., Mao, C., Xiang, Y., Wu, S., Cheung, K.M.C., and Yeung, K.W.K. (2021). Rapid bacterial elimination achieved by sonodynamic Au@Cu_2O hybrid nanocubes. Nanoscale *13*, 15699–15710. https://doi.org/10.1039/d1nr04512a.
77. He, T., Cao, C., Xu, Z., Li, G., Cao, H., Liu, X., Zhang, C., and Dong, Y. (2017). A comparison of micro-CT and histomorphometry for evaluation of osseointegration of PEO-coated titanium implants in a rat model. Sci. Rep. *7*, 16270. https://doi.org/10.1038/s41598-017-16465-4.
78. Shen, J., Wang, W., Zhai, X., Chen, B., Qiao, W., Li, W., Li, P., Zhao, Y., Meng, Y., Qian, S., et al. (2019). 3D-printed nanocomposite scaffolds with tunable magnesium ionic microenvironment induce in situ bone tissue regeneration. Appl. Mater. Today *16*, 493–507. https://doi.org/10.1016/j.apmt.2019.07.012.